International Journal of Solids and Structures 338 (2026) 114092

Contents lists available at ScienceDirect

International Journal of Solids and Structures

journal homepage: www.elsevier.com/locate/ijsolstr

Computational analysis of fracture and fatigue in overmolded thermoplastic composites: Time-homogenized viscoplasticity, cohesive fracture and processing effects

P. Hofman *, F.P. van der Meer, L.J. Sluys

Delft University of Technology, Faculty of Civil Engineering and Geosciences, Delft, PO Box 5048, 2600 GA, The Netherlands

ARTICLE INFO

Dataset link: https://doi.org/10.4121/90f36631-80eb-4d63-b0ac-aad708024e2e

Keywords:
Thermoplastic composites
Overmolding
Processing effects
Fatigue
Time-homogenization

ABSTRACT

A numerical framework is presented for simulating fracture and fatigue in a T-section, cut from an overmolded thermoplastic composite panel made of CF/PEEK. The framework combines a cohesive zone model for the overmolded interface with an anisotropic viscoplasticity model for the laminate and accounts for processing effects. For high-cycle fatigue analyses, a two-scale time-homogenized version of the viscoplasticity model is derived. The numerical framework is applied to the analysis of a rib pull-off test and is used to gain insights into the influence on the short- and long-term response of two typical processing effects: out-of-plane deformations of the laminate that occur during thermoforming and non-uniform healing profiles resulting from spatially varying thermal histories. Furthermore, the effects of various modeling assumptions are studied, such as modeling the local fiber orientations of each ply in the laminate with a mesoscopic ply-by-ply approach, the effect of viscoplastic deformations in the laminate, the influence of non-uniform local stress ratios, and the effect of the boundary conditions. The analyses demonstrate that the framework is capable of efficiently simulating a large number of cycles. The simulation results show that the local wrinkles in the laminate as a result of thermoforming have a significant effect on the mechanical response, especially under cyclic loading. Moreover, accounting for viscoplastic deformations appears more important when high degrees of bonding of the overmolded interface are achieved. Finally, it is shown that changes to the boundary conditions have a significant effect on the short and long-term response of the T-section, challenging the validity of the test for characterizing fracture and fatigue properties of the overmolded interface.

1. Introduction

Thermoplastic overmolding is a manufacturing technique that combines thermoforming with injection molding. During this process, a thermoplastic laminate, made of unidirectional or long-fiber woven plies, is heated above the melt temperature and subsequently formed into the desired shape (thermoforming). After thermoforming, a reinforcing rib, often made of the same polymer matrix and optionally reinforced with short fibers, is overinjected onto the laminate.

This manufacturing technique is gaining more interest in recent years since it has the potential to significantly contribute to lightweighting in the automotive and aerospace sectors. In particular, overmolding enables near net shape manufacturing of composite parts with fast processing cycles and complex geometries without additional fasteners that add weight. However, a challenging aspect is that the mechanical performance of the final product depends on the processing parameters (Valverde et al., 2018; Akkerman et al., 2020; Fu et al., 2022; Jiang et al., 2022; Neveu et al., 2022; Parsons et al., 2025). The understanding of the relation between processing and performance is currently not at a mature level, which is preventing the wide-spread use of overmolded thermoplastic composite parts in transportation industries.

There are two main processing effects that influence the mechanical performance of the final product. Firstly, the laminate deforms locally out of plane during thermoforming, leading to fibers and polymer resin that enter the mold cavity (Akkerman et al., 2020). After thermoforming, this results in wrinkles in the laminate and after injection molding, these plies protrude into the rib structure (see Fig. 1). Secondly, during overmolding, the temperature distribution is non-uniform due to different temperatures of the overmolding compound, the laminate and the mold tool. To obtain a strong interface, a high temperature for a sufficient duration is necessary to allow polymer chains to move across the interface (a process known as *interdifussion*). The difference

* Corresponding author.
E-mail address: P.Hofman@tudelft.nl (P. Hofman).

https://doi.org/10.1016/j.ijsolstr.2026.114092
Received 13 January 2026; Received in revised form 7 April 2026; Accepted 13 May 2026
Available online 19 May 2026

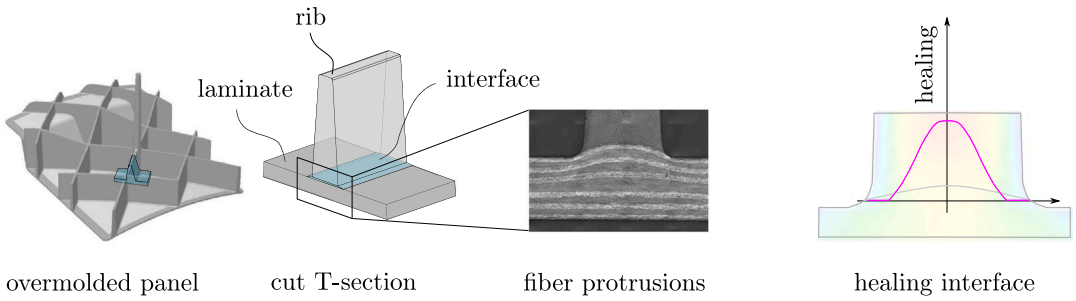

Fig. 1. Processing effects in an overmolded panel. First and third picture are adapted from Akkerman et al. (2020) and Valverde (2021), respectively.

in thermal histories leads to varying levels of healing and consequently non-uniform fracture properties along the overmolded interface.

Since the processing parameters have a large influence on the mechanical response of thermoplastic overmolded composite parts, optimizing manufacturing procedures and part performance is not straightforward, resulting in time-consuming and costly trial-and-error experimental campaigns. An important factor for performance assessment is determining the quality of the overmolded interface, *e.g.* in terms of strength. This is often done through mechanical testing of a T-section (Joppich et al., 2017; Liebsch et al., 2019; Valverde, 2021; Giusti and Lucchetta, 2023; Song et al., 2024; Parsons et al., 2025), cut from an overmolded panel (see Fig. 1). However, specimen dimensions and boundary conditions influence the measured strength of the T-section (Song et al., 2024; Daghia et al., 2025), questioning the validity of the test for its use in determining the strength of the interface. In contrast to time-consuming and costly experimental testing procedures, numerical models allow for a large number of virtual experiments to predict the effects of processing on the performance and to provide insights into the consequences of certain test set-ups. Therefore, for reaching the full potential of overmolded thermoplastic composites in aerospace and automotive industries, it is crucial to develop accurate, efficient and robust simulation tools.

So far, only a small number of studies have focused on numerically simulating failure under static loading in overmolded T-sections (Giusti and Lucchetta, 2020; Valverde, 2021; Song et al., 2024). In these works, several assumptions have been made: the numerical models consider the laminate as a single homogenized material and do not take into account the non-uniformly distributed local fiber orientations. Furthermore, all material nonlinearities are lumped at the overmolded interface and the effects of viscoplastic deformations, which typically occur in thermoplastic composites, are not taken into account. Moreover, studies have focused on short-term (static) performance assessments, while long-term performance (fatigue and creep) of overmolded thermoplastic composites has not been investigated.

In this work, we set aside the aforementioned simplifying assumptions and present the first modeling framework for simulating both fracture and fatigue in overmolded thermoplastic composites. The framework builds on previous works (Hofman et al., 2024a,b), where a progressive fatigue framework for multidirectional composites was presented. In this article, we extend the previous framework for simulating failure in overmolded composites, taking into account viscoplastic deformations and processing effects. Viscoplastic deformations accumulate during fatigue cycles and affect the local stress ratios at the overmolded interface during a cyclic test. To account for these effects, a recently developed anisotropic viscoplasticity model (Hofman et al., 2025) is included in the framework and a two-scale time-homogenized version is derived for efficient high-cycle fatigue analyses. In comparison to earlier numerical analyses on overmolded T-sections (Valverde, 2021; Song et al., 2024) for static loading, new features of the present numerical framework for simulating both fracture and fatigue are:

- A fatigue mixed-mode cohesive zone model (Dávila, 2020; Dávila et al., 2020) is employed for simulating cohesive fracture and fatigue at the overmolded interface.
- A recently developed transversely isotropic viscoplasticity model for thermoplastic composites (Hofman et al., 2025) is used to account for the effects of viscoplastic deformations in the laminate.
- A two-scale version of the viscoplasticity model is developed with temporal homogenization to efficiently simulate a large number of cycles under high-cycle fatigue.
- A ply-by-ply modeling approach is used for the laminate and the process-induced mesoscopic geometry, including the effect on the fiber orientation, is taken into account. With this approach, the effect of wrinkles due to thermoforming is studied.

With the numerical framework, overmolded T-sections made of CF/PEEK are simulated under quasi-static and cyclic loading to gain insight into the processing effects on both the short- and long-term performance of overmolded composites. In the numerical analyses, special attention is given to the effects of varying healing profiles at the overmolded interface and process-induced deformations on the mechanical response of the specimen. In addition, the effects of modeling assumptions, such as process-induced wrinkles and the importance of viscoplastic deformations in the laminate are investigated. Finally, the effects of the boundary conditions are discussed.

This paper is outlined as follows. Firstly, the constitutive models for the overmolded interface, the laminate and the rib are discussed in Section 2. Subsequently, a two-scale version of the viscoplasticity model is derived in Section 3. In Section 4, the computational modeling approach of the overmolded T-section is outlined and the results are discussed in Section 5. Finally, conclusions are presented at the end of the paper.

2. Constitutive models

The constitutive models for the T-section are presented in this section. In this manuscript, we use Dávila's cyclic cohesive zone model (Dávila, 2020; Dávila et al., 2020), summarized in Section 2.1, for simulating fracture and fatigue at the overmolded interface of the T-section. The performance of Dávila's model has been demonstrated previously on fracture specimens (Dávila, 2020; Dávila et al., 2020) and on quasi-isotropic open-hole laminates (Hofman et al., 2024b). In Section 2.2, a recently developed transversely isotropic viscoplasticity model for the continuous fiber reinforced laminate (Hofman et al., 2025) is summarized. Furthermore, the rib is considered transversely isotropic elastic and follows the same constitutive relations of the laminate (Section 2.2.3), albeit without viscoplastic deformations.

2.1. Fatigue cohesive zone model

The overmolded interface is modeled with a cycle-dependent cohesive zone model (Dávila, 2020; Dávila et al., 2020). The model is formulated in a local coordinate frame aligned with the crack plane. The traction vector $\mathbf{t} = \left[t_n, t_{s1}, t_{s2}\right]^{\mathrm{T}}$ is computed from the displacement jump $[\![\mathbf{u}]\!] = \left[[\![u]\!]_n, [\![u]\!]_{s1}, [\![u]\!]_{s2}\right]^{\mathrm{T}}$ as

$$\mathbf{t} = (\mathbf{I} - d\,\mathbf{P})\mathbf{K}[\![\mathbf{u}]\!] \tag{1}$$

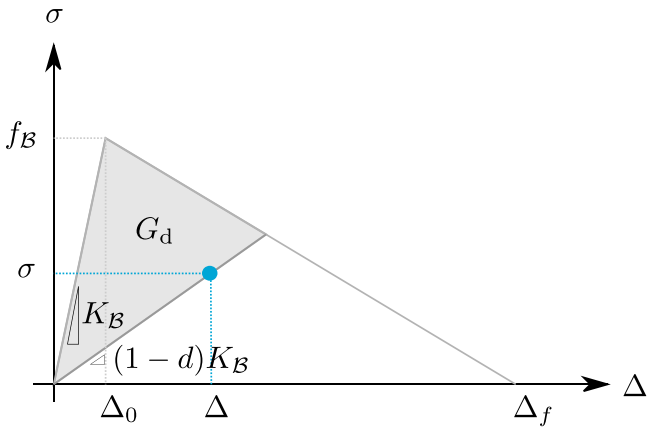

Fig. 2. Mixed-mode equivalent traction-separation relation: the cyclic response (•) is inside the quasi-static envelope.

where $d \in (0,1)$ is a scalar damage variable, $\mathbf{K}$ is the dummy stiffness matrix and $\mathbf{P}$ is a selection matrix. The matrices $\mathbf{K}$ and $\mathbf{P}$ are given as

$$\mathbf{K} = \begin{bmatrix} K_n & 0 & 0 \\ 0 & K_{sh} & 0 \\ 0 & 0 & K_{sh} \end{bmatrix}, \qquad \mathbf{P} = \begin{bmatrix} \frac{\langle [\![u]\!]_n \rangle}{[\![u]\!]_n} & 0 & 0 \\ 0 & 1 & 0 \\ 0 & 0 & 1 \end{bmatrix} \tag{2}$$

where K_n and K_{sh} are the normal and shear dummy stiffnesses, respectively. The Macaulay operator $\langle \bullet \rangle = \max(0, \bullet)$ in the selection matrix $\mathbf{P}$ prevents interfacial penetration. The model is formulated in terms of an mixed-mode equivalent traction-separation relation:

$$\sigma = (1-d) K_{\mathcal{B}} \Delta \tag{3}$$

which is illustrated in Fig. 2. In Eq. (3), σ is the mixed-mode equivalent traction, $K_{\mathcal{B}}$ is the mode-dependent dummy stiffness and Δ is the mixed-mode equivalent displacement jump:

$$\sigma = \sqrt{\langle t_n \rangle^2 + t_{s1}^2 + t_{s2}^2} \tag{4}$$

$$K_{\mathcal{B}} = K_n(1-\mathcal{B}) + \mathcal{B} K_{sh} \tag{5}$$

$$\Delta = \frac{K_n \langle [\![u]\!]_n \rangle^2 + K_{sh} [\![u]\!]_{sh}^2}{\sqrt{K_n^2 \langle [\![u]\!]_n \rangle^2 + K_{sh}^2 [\![u]\!]_{sh}^2}} \tag{6}$$

where $[\![u]\!]_{sh}^2 = [\![u]\!]_{s1}^2 + [\![u]\!]_{s2}^2$. Furthermore, $\mathcal{B}$ is defined as:

$$\mathcal{B} = \frac{K_{sh} [\![u]\!]_{sh}^2}{K_n \langle [\![u]\!]_n \rangle^2 + K_{sh} [\![u]\!]_{sh}^2} \tag{7}$$

and is a measure of mode-mixity. An energy-based damage variable $\mathcal{D}$ is introduced as state variable which can only increase in time, *i.e.* $\mathcal{D}(t) = \max_{0 \le \tau \le t}(\mathcal{D}(\tau))$. The damage variable $\mathcal{D}$ is defined as:

$$\mathcal{D} \equiv \frac{G_{\mathrm{d}}}{G_{\mathrm{c}}} \tag{8}$$

where G_{d} is the dissipated energy (see Fig. 2) and G_{c} is the mixed-mode fracture energy.

Furthermore, $f_{\mathcal{B}}$ in Fig. 2 is the mixed-mode equivalent static strength, which is computed as

$$f_{\mathcal{B}} = \sqrt{(K_n(1-\mathcal{B}) + \mathcal{B} K_{sh}) \left[f_n^2 / K_n + (f_{sh}^2 / K_{sh} - f_n^2 / K_n) \mathcal{B}^{\eta_{\mathrm{BK}}} \right]} \tag{9}$$

where f_n, f_{sh} are the tensile strength and shear strength, respectively, and η_{BK} is the Benzeggagh–Kenane mixed-mode interaction parameter (Benzeggagh and Kenane, 1996).

$\mathcal{D}$ in Eq. (8) evolves under static loading and under cyclic loading. The calculation of $\mathcal{D}$ for each loading condition is explained in Sections 2.1.1 and 2.1.2, respectively.

2.1.1. Quasi-static damage evolution

Under quasi-static loading, $\mathcal{D}$ is computed as

$$\mathcal{D} = \frac{\Delta - \Delta_0}{\Delta_f - \Delta_0} \tag{10}$$

where Δ_0 and Δ_f are the mixed-mode equivalent displacement jumps at fracture initiation and full decohesion:

$$\Delta_0 = \sqrt{\frac{K_n ([\![u]\!]_n^0)^2 + \left(K_{sh} ([\![u]\!]_{sh}^0)^2 - K_n ([\![u]\!]_n^0)^2 \right) \mathcal{B}^{\eta_{\mathrm{BK}}}}{K_{\mathcal{B}}}} \tag{11}$$

$$\Delta_f = \frac{K_n [\![u]\!]_n^0 [\![u]\!]_n^f + \left(K_{sh} [\![u]\!]_{sh}^0 [\![u]\!]_{sh}^f - K_n [\![u]\!]_n^0 [\![u]\!]_n^f \right) \mathcal{B}^{\eta_{\mathrm{BK}}}}{K_{\mathcal{B}} \Delta_0} \tag{12}$$

The corresponding jump components are given by

$$[\![u]\!]_n^0 = \frac{f_n}{K_n}, \qquad [\![u]\!]_n^f = \frac{2G_{Ic}}{f_n} \tag{13}$$

$$[\![u]\!]_{sh}^0 = \frac{f_{sh}}{K_{sh}}, \qquad [\![u]\!]_{sh}^f = \frac{2G_{IIc}}{f_{sh}} \tag{14}$$

where $G_{\mathrm{Ic,d}}$ and $G_{\mathrm{IIc,d}}$ are mode-I and mode-II fracture energies, respectively. Furthermore, the damage variable d is computed as

$$d = 1 - \frac{(1-\mathcal{D})\Delta_0}{\mathcal{D}\Delta_f + (1-\mathcal{D})\Delta_0} \tag{15}$$

2.1.2. Fatigue damage evolution

Under cyclic loading, $\mathcal{D}$ evolves with number of cycles N. The damage rate $\mathrm{d}\mathcal{D}/\mathrm{d}N$ is described by the following differential equation (Dávila et al., 2020)

$$\frac{\mathrm{d}\mathcal{D}}{\mathrm{d}N} = \frac{1}{\gamma} \frac{(1-\mathcal{D})^{\beta-p}}{E^{\beta}(p+1)} \left(\frac{\Delta}{\Delta^*} \right)^{\beta} \tag{16}$$

where Δ^* is the displacement jump at which quasi-static damage develops, given as

$$\Delta^* = \mathcal{D}(\Delta_f - \Delta_0) + \Delta_0 \tag{17}$$

The parameters in Eq. (16) can be fitted to ensure that the evolution of $\mathcal{D}$ at constant stress level leads to failure after N cycles, as described by an S-N curve (see Fig. 3) (Dávila, 2020). In Eq. (16), γ and p are model parameters and β is given as

$$\beta = \frac{-7\eta}{\log E} \tag{18}$$

where η is a parameter that controls the curved shape of the S-N curve in the low-cycle regime. Furthermore, E is the relative endurance limit, defined as the ratio of the endurance limit σ_{end} to the static mixed-mode strength $f_{\mathcal{B}}$ and is given as

$$E = \frac{2C\epsilon}{C\epsilon + 1 + R(C\epsilon - 1)} \tag{19}$$

where R is the local stress ratio and ϵ is the endurance limit at $R = -1$. Furthermore, C takes into account the mode-mixity and follows an empirical relation (Juvinall and Marshek, 2012):

$$C = 1 - 0.42\mathcal{B} \tag{20}$$

Under cyclic loading, $\mathcal{D}$ is computed with an implicit time integration scheme, using the trapezoidal rule (Hofman et al., 2024a):

$$\mathcal{D}^{(n)} = \mathcal{D}^{(n-1)} + \frac{\Delta N}{2} \left(\frac{\mathrm{d}\mathcal{D}}{\mathrm{d}N}^{(n-1)} + \frac{\mathrm{d}\mathcal{D}}{\mathrm{d}N}^{(n)} \right) \tag{21}$$

where the damage rates $\mathrm{d}\mathcal{D}/\mathrm{d}N^{(n-1)}$ and $\mathrm{d}\mathcal{D}/\mathrm{d}N^{(n)}$ correspond to the previous and the current time step, respectively. Eq. (21) is a nonlinear equation, which is iteratively solved with Newton's method.

Furthermore, to ensure that the traction-separation response is inside the quasi-static envelope, $\mathcal{D}$ is determined as the maximum of the damage computed with Eq. (21) and quasi-static damage with Eq. (10):

$$\mathcal{D} = \max \left(\frac{\Delta - \Delta_0}{\Delta_f - \Delta_0}, \mathcal{D} \right) \tag{22}$$

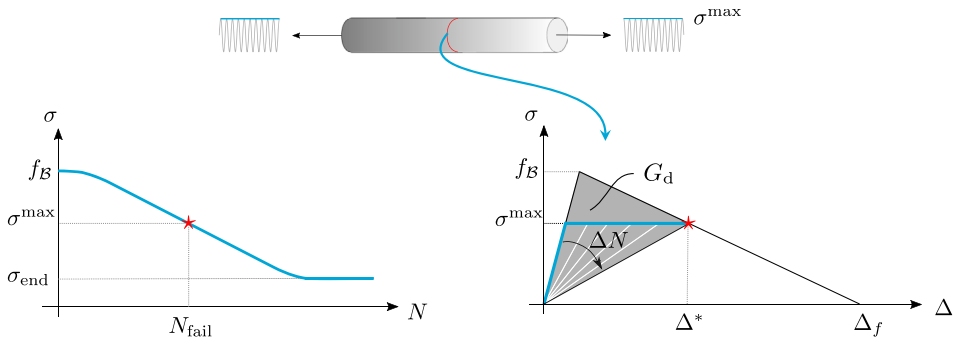

Fig. 3. Failure with the cohesive zone model is described by an S-N curve: at maximum stress level $\sigma^{\max}$, stiffness degrades with each cycle increment ΔN until the traction-separation response reaches the quasi-static softening line after N cycles $(\Delta^\star, \sigma^{\max})$. Upon further increase in cycles, the material cannot sustain the load anymore and is considered to have failed (indicated with $\star$).

With D known, the damage variable d in Eq. (3) is computed through Eq. (15). The consistent tangent stiffness matrix for implicit finite element analysis is presented in Hofman et al. (2024a).

2.2. Transversely isotropic viscoplasticity model

The laminate is modeled with a transversely isotropic viscoplasticity model for thermoplastic composites (Hofman et al., 2025), a recently developed constitutive model based on the Eindhoven Glassy Polymer model (Tervoort et al., 1996, 1997; van Breemen et al., 2011). The Cauchy stress is composed of N_{m} nonlinear spring-dashpots, denoted as *modes*:

$$\boldsymbol{\sigma} = \sum_{i}^{N_{\text{m}}} \boldsymbol{\sigma}_i \tag{23}$$

where $\boldsymbol{\sigma}_i$ is the Cauchy stress in mode i. By accounting for multiple modes, a continuous spectrum of relaxation times for glassy polymers is approximated (Tervoort et al., 1996; van Breemen et al., 2011). The rheological model is shown in Fig. 4. The total deformation gradient $\mathbf{F}$ is multiplicatively decomposed (Kröner, 1959; Lee, 1969) into an elastic $\mathbf{F}_{ei}$ and a plastic $\mathbf{F}_{pi}$ deformation gradient:

$$\mathbf{F} = \mathbf{F}_{ei} \cdot \mathbf{F}_{pi} \tag{24}$$

The decomposition and corresponding configurations are depicted in Fig. 5. The plastic velocity gradient is additively decomposed into the rate of plastic deformation tensor $\hat{\mathbf{D}}_{pi}$ and the plastic material spin $\hat{\mathbf{W}}_{\text{p}}$:

$$\hat{\mathbf{L}}_{pi} = \dot{\mathbf{F}}_{pi} \cdot \mathbf{F}_{pi}^{-1} = \underbrace{\left(\dot{\mathbf{F}}_{pi} \cdot \mathbf{F}_{pi}^{-1}\right)^{\text{sym}}}_{\hat{\mathbf{D}}_{pi}} + \underbrace{\left(\dot{\mathbf{F}}_{pi} \cdot \mathbf{F}_{pi}^{-1}\right)^{\text{skw}}}_{\hat{\mathbf{W}}_{pi}} \tag{25}$$

where the plastic material spin $\hat{\mathbf{W}}_{pi}$ is set to zero to remove the issue of non-uniqueness of Eq. (24). As a result, the evolution of $\mathbf{F}_{pi}$ reads

$$\dot{\mathbf{F}}_{pi} = \hat{\mathbf{D}}_{pi} \cdot \mathbf{F}_{pi} \tag{26}$$

where $\hat{\mathbf{D}}_{pi}$ is described by the following flow rule

$$\hat{\mathbf{D}}_{pi} = \dot{\gamma}_{pi} \hat{\mathbf{N}}_{pi} \tag{27}$$

In this equation, $\dot{\gamma}_{pi}$ is the equivalent plastic strain rate and $\hat{\mathbf{N}}_{pi}$ is the direction of plastic flow. The equivalent plastic strain rate reads

$$\dot{\gamma}_{pi} = \frac{\bar{\Sigma}_i}{\eta_i} \tag{28}$$

where $\bar{\Sigma}_i$ is the equivalent stress in mode i and the viscosity η_i in each mode is given as

$$\eta_i = \eta_{0i}\, a_\sigma \tag{29}$$

where a_σ is the so-called *stress shift factor* and η_{0i} is the initial viscosity of mode i. In this formulation, the viscosity starts with a high value (representing solid-like behavior) and reduces when stress is applied through a_σ (representing fluid-like behavior). The stress shift factor depends on the total equivalent stress $\bar{\sigma}$ through a transverse pressure-extended Eyring relation:

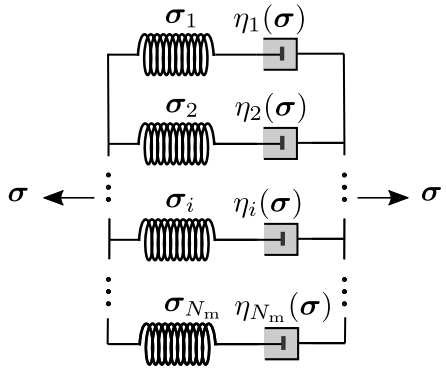

Fig. 4. Rheological model of the transversely isotropic viscoplasticity model.

$$a_\sigma = \frac{\bar{\sigma}/\sigma_0}{\sinh\left(\bar{\sigma}/\sigma_0\right)} \exp\left(-\mu_{\text{p}} \frac{p_{\text{m}}}{\sigma_0}\right) \tag{30}$$

where σ_0 is a model parameter that determines the exponential decrease of the viscosity, μ_{p} is the pressure dependency parameter and p_{m} is a measure of pressure in the polymer matrix. The quantities $\bar{\Sigma}_i$, $\bar{\sigma}$ and p_{m} take into account the transverse isotropy in the plasticity relations and are defined below.

2.2.1. Total equivalent stress

An initial fiber vector $\boldsymbol{a}_0$ (see Fig. 5) is introduced to represent transverse isotropy and its evolution is described by Eq. (24):

$$\boldsymbol{a} = \mathbf{F}_{ei} \cdot \hat{\boldsymbol{a}}_i = \mathbf{F}_{ei} \cdot \mathbf{F}_{pi} \cdot \boldsymbol{a}_0 = \mathbf{F} \cdot \boldsymbol{a}_0 \tag{31}$$

where $\boldsymbol{a}_0$, $\hat{\boldsymbol{a}}_i$ and $\boldsymbol{a}$ are the fiber vectors in the *initial*, *intermediate* and *current* configurations, respectively. Through Eq. (31), the change of orientation of the transversely isotropic plane is taken into account. Furthermore, the Cauchy stress is decomposed into a plasticity inducing $\boldsymbol{\sigma}^{\text{pind}}$ and a remaining part (Spencer, 1972, 1987)

$$\boldsymbol{\sigma}^{\text{pind}} = \boldsymbol{\sigma} - (p\, \mathbf{I} + \sigma_{\text{f}}\, \bar{\mathbf{A}}) \tag{32}$$

where p is the pressure and σ_{f} is the part of the Cauchy stress projected onto the fiber direction that exceeds the pressure. Furthermore, $\bar{\mathbf{A}} = \bar{\boldsymbol{a}} \otimes \bar{\boldsymbol{a}}$ is a structural tensor, with $\bar{\boldsymbol{a}} = \boldsymbol{a}/\|\boldsymbol{a}\|$ being the unit vector in the current configuration. The plasticity inducing stress, as defined in Eq. (32), is determined from the total stress as:

$$\boldsymbol{\sigma}^{\text{pind}} = \mathbb{P} : \boldsymbol{\sigma} \tag{33}$$

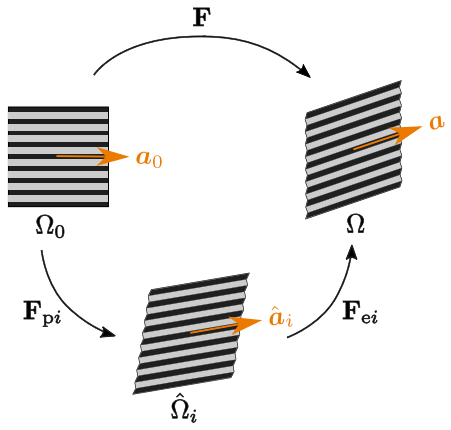

Fig. 5. Schematic of the multiplicative decomposition of the total deformation into an elastic and plastic deformation with the corresponding configurations: *initial* (Ω_0), *intermediate* ($\hat{\Omega}_i$) and *current* configuration (Ω).

where fourth-order tensor $\mathbb{P}$ is defined as

$$\mathbb{P} = \mathbb{I} - \frac{1}{2}\mathbf{I}\otimes\mathbf{I} - \frac{3}{2}\bar{\mathbf{A}}\otimes\bar{\mathbf{A}} + \frac{1}{2}\left(\bar{\mathbf{A}}\otimes\mathbf{I} - \mathbf{I}\otimes\bar{\mathbf{A}}\right) \tag{34}$$

with $\mathbb{I}$ the fourth-order identity tensor. The following three invariants for transverse isotropy are introduced (Vogler et al., 2013)

$$I_1 = \frac{1}{2}\,\mathrm{tr}\left[\boldsymbol{\sigma}^{\mathrm{pind}}\cdot\boldsymbol{\sigma}^{\mathrm{pind}}\right] - \bar{\boldsymbol{a}}\cdot\left[\boldsymbol{\sigma}^{\mathrm{pind}}\cdot\boldsymbol{\sigma}^{\mathrm{pind}}\right]\cdot\bar{\boldsymbol{a}} \tag{35}$$

$$I_2 = \bar{\boldsymbol{a}}\cdot\left[\boldsymbol{\sigma}^{\mathrm{pind}}\cdot\boldsymbol{\sigma}^{\mathrm{pind}}\right]\cdot\bar{\boldsymbol{a}} \tag{36}$$

$$I_3 = \mathrm{tr}\left[\boldsymbol{\sigma}\right] - \bar{\boldsymbol{a}}\cdot\boldsymbol{\sigma}\cdot\bar{\boldsymbol{a}} \tag{37}$$

where I_1 is associated with transverse shear, I_2 with longitudinal shear and I_3 with transverse biaxial tension/compression. The equivalent stress is defined as a function of invariants I_1 and I_2

$$\bar{\sigma} = \sqrt{2\left(I_1 + \alpha_2 I_2\right)} \tag{38}$$

where α_2 is a model parameter. The third invariant is used to define p_{m} in Eq. (30):

$$p_{\mathrm{m}} = I_3 \tag{39}$$

2.2.2. Equivalent stress in each mode

For defining the equivalent stress in each mode $\bar{\Sigma}_i$, a Mandel-like stress tensor (Mandel, 1972) is introduced:

$$\boldsymbol{\Sigma}_i = \mathbf{F}_{ei}^{\mathrm{T}}\cdot\boldsymbol{\sigma}_i\cdot\mathbf{F}_{ei}^{-\mathrm{T}} \tag{40}$$

which is work-conjugate to the rate of plastic deformation $\hat{\mathbf{D}}_{pi}$ (Eq. (27)). In general, $\boldsymbol{\Sigma}_i$ is a non-symmetric tensor. To ensure that $\hat{\mathbf{D}}_{pi}$ is symmetric, only the symmetric part $\boldsymbol{\Sigma}_i^{\mathrm{sym}} = {}^1\!/_2\left(\boldsymbol{\Sigma}_i^{\mathrm{T}} + \boldsymbol{\Sigma}_i\right)$ determines the direction of plastic flow (Rodrigues Lopes et al., 2022).

The plasticity inducing part $\boldsymbol{\Sigma}_i^{\mathrm{pind}}$ is obtained from $\boldsymbol{\Sigma}_i^{\mathrm{sym}}$ through (Rodrigues Lopes et al., 2022; Hofman et al., 2025):

$$\boldsymbol{\Sigma}_i^{\mathrm{pind}} = \hat{\mathbb{P}}_i : \boldsymbol{\Sigma}_i^{\mathrm{sym}} \tag{41}$$

with fourth-order tensor $\hat{\mathbb{P}}_i$

$$\hat{\mathbb{P}}_i = \mathbb{I} - \frac{1}{2}\mathbf{I}\otimes\mathbf{I} - \frac{3}{2}\hat{\mathbf{A}}_i\otimes\hat{\mathbf{A}}_i + \frac{1}{2}\left(\hat{\mathbf{A}}_i\otimes\mathbf{I} - \mathbf{I}\otimes\hat{\mathbf{A}}_i\right) \tag{42}$$

The invariants for each mode read

$$\hat{I}_{1i} = \frac{1}{2}\,\mathrm{tr}\left[\boldsymbol{\Sigma}_i^{\mathrm{pind}}\cdot\boldsymbol{\Sigma}_i^{\mathrm{pind}}\right] - \hat{\boldsymbol{a}}_i\cdot\left[\boldsymbol{\Sigma}_i^{\mathrm{pind}}\cdot\boldsymbol{\Sigma}_i^{\mathrm{pind}}\right]\cdot\hat{\boldsymbol{a}}_i \tag{43}$$

$$\hat{I}_{2i} = \hat{\boldsymbol{a}}_i\cdot\left[\boldsymbol{\Sigma}_i^{\mathrm{pind}}\cdot\boldsymbol{\Sigma}_i^{\mathrm{pind}}\right]\cdot\hat{\boldsymbol{a}}_i \tag{44}$$

and the equivalent stress $\bar{\Sigma}_i$ is defined as

$$\bar{\Sigma}_i = \sqrt{2\left(\hat{I}_{1i} + \alpha_2\hat{I}_{2i}\right)} \tag{45}$$

The direction of plastic flow is described through an associated flow rule

$$\mathbf{N}_{pi} = \frac{\partial\bar{\Sigma}_i}{\partial\boldsymbol{\Sigma}_i^{\mathrm{sym}}} = \frac{1}{\bar{\Sigma}_i}\left[\frac{\partial\hat{I}_{1i}}{\partial\boldsymbol{\Sigma}_i^{\mathrm{sym}}} + \alpha_2\frac{\partial\hat{I}_{2i}}{\partial\boldsymbol{\Sigma}_i^{\mathrm{sym}}}\right] \tag{46}$$

where

$$\frac{\partial\hat{I}_{1i}}{\partial\boldsymbol{\Sigma}_i^{\mathrm{sym}}} = \left[\left(\mathbf{I} - \hat{\mathbf{A}}_i\right)\cdot\boldsymbol{\Sigma}_i^{\mathrm{pind}} - \boldsymbol{\Sigma}_i^{\mathrm{pind}}\cdot\hat{\mathbf{A}}_i\right] : \hat{\mathbb{P}}_i \tag{47}$$

$$\frac{\partial\hat{I}_{2i}}{\partial\boldsymbol{\Sigma}_i^{\mathrm{sym}}} = \left[\hat{\mathbf{A}}_i\cdot\boldsymbol{\Sigma}_i^{\mathrm{pind}} + \boldsymbol{\Sigma}_i^{\mathrm{pind}}\cdot\hat{\mathbf{A}}_i\right] : \hat{\mathbb{P}}_i \tag{48}$$

2.2.3. Transversely isotropic hyperelasticity

The Cauchy stress in each mode is computed with a hyperelastic model based on Bonet and Burton (1998). The stress $\boldsymbol{\sigma}_i$ is decomposed in an isotropic (iso) and a transversely isotropic part (trn):

$$\boldsymbol{\sigma}_i = \boldsymbol{\sigma}_{\mathrm{iso},i} + \boldsymbol{\sigma}_{\mathrm{trn},i} \tag{49}$$

with

$$\begin{aligned}\boldsymbol{\sigma}_{\mathrm{iso},i} &= \frac{\mu_i}{J_{ei}}\left(\mathbf{B}_{ei} - \mathbf{I}\right) + \lambda_i(J_{ei} - 1)\mathbf{I}\\ J_{ei}\boldsymbol{\sigma}_{\mathrm{trn},i} &= 2\beta_i(\xi_2 - 1)\mathbf{B}_{ei} + 2\left[\alpha_i + \beta_i(\xi_{1i} - 3) + 2\gamma_i(\xi_2 - 1)\right]\boldsymbol{a}\otimes\boldsymbol{a}\\ &\quad - \alpha_i\left(\mathbf{B}_{ei}\cdot\boldsymbol{a}\otimes\boldsymbol{a} + \boldsymbol{a}\otimes\mathbf{B}_{ei}\cdot\boldsymbol{a}\right)\end{aligned} \tag{50}$$

where $\mathbf{B}_{ei} = \mathbf{F}_{ei}\cdot\mathbf{F}_{ei}^{\mathrm{T}}$ is the elastic left Cauchy–Green deformation tensor, $J_{ei} = \det\left(\mathbf{F}_{ei}\right)$ and ξ_{1i} and ξ_2 are given as

$$\xi_{1i} = \mathrm{tr}\left(\mathbf{B}_{ei}\right) \tag{51}$$

$$\xi_2 = \boldsymbol{a}\cdot\boldsymbol{a} \tag{52}$$

Furthermore, $\lambda_i, \mu_i, \alpha_i, \beta_i$ and γ_i are elasticity constants that are determined from Young's moduli, shear moduli and Poisson's ratios $\{E_{1i}, E_{2i}, G_{12i}, \nu_{12i}, \nu_{23i}\}$ (Kovačević and van der Meer, 2022):

$$\begin{aligned} n_i &= \frac{E_{2i}}{E_{1i}}\\ m_i &= 1 - \nu_{23i} - 2n\nu_{12i}^2\\ \lambda_i &= E_{2i}\frac{\nu_{23i} + n_i\,\nu_{12i}^2}{m_i(1 + \nu_{23i})}\\ \mu_i &= \frac{E_{2i}}{2(1 + \nu_{23i})}\\ \alpha_i &= \mu_i - G_{12i}\\ \beta_i &= \frac{E_{2i}\left(\nu_{12i} + \nu_{23i}\nu_{12i} - \nu_{23i} - n\nu_{12i}^2\right)}{4m_i(1 + \nu_{23i})}\\ \gamma_i &= \frac{E_{1i}(1 - \nu_{23i})}{8m_i} - \frac{\lambda_i + 2\mu_i}{8} + \frac{\alpha_i}{2} - \beta_i \end{aligned} \tag{53}$$

The implementation details and derivation of the consistent tangent modulus can be found in Hofman et al. (2025).

3. Time-homogenization of viscoplasticity

For accurate fatigue and fracture analyses of thermoplastic composites, it is important to take viscoplastic deformations into account. However, simulating every cycle in high-cycle fatigue, with multiple time steps per cycle, is computationally too expensive. Therefore, the concept of time-homogenization (Yu and Fish, 2002; Oskay and Fish, 2004; Haouala and Doghri, 2015; Rocha et al., 2019; Kovačević et al., 2024) is used to simulate a large number of cycles with a small number of time steps.

3.1. Effective time concept

In the present model, we separate the bulk behavior, which is viscoplastic (time dependent), from the response at the overmolded

interface, which is cohesive (cycle dependent). The fatigue life of thermoplastic composites, in the plasticity-controlled regime, is frequency independent (Kanters et al., 2016; Kovačević et al., 2024). Therefore, the cyclic response in the bulk can be considered to be a special case of creep. When the load is kept constant, the maximum amount of viscoplastic flow develops. On the other hand, during cyclic loading, only a fraction of the period T is spent at high stress levels and therefore less viscoplastic deformations accumulate. This portion of the time can be considered to be an *effective time* T_{eff}.

The concept of *effective time* can be used to speed up the computations significantly. To this end, two time scales are introduced: (*i*) a rapidly varying *micro time* t_μ that runs during a load period T and (*ii*) a slowly varying *macro time* t_{M}. For solving the cyclic response, the problem is split into a microchronogical (t_μ) and macrochronological (t_{M}) boundary value problem. For the microchronological problem, the cyclic load is explicitly modeled. During t_μ, it is assumed that there is not enough time for viscoplastic deformations to evolve and therefore, an elastic material update, with *frozen* plastic deformation, suffices. On the other hand, during t_{M} the full viscoplastic update is necessary and the time integration of Eq. (26) is performed with the effective time period T_{eff}, instead of the real time T.

The effective time should incorporate the effect of the cyclic load. This can be achieved by choosing a representative state variable that measures the amount of viscoplastic flow. For the present viscoplasticity model, the equivalent plastic strain rate $\dot{\gamma}_{\text{p}}$ is used, following Kovačević et al. (2024). Subsequently, the effective time is determined such that

$$\dot{\gamma}_{\text{p,M}}\, T_{\text{eff}} = \int_T \dot{\gamma}_{\text{p},\mu}\mathrm{d}t_\mu \iff T_{\text{eff}} = \frac{\int_T \dot{\gamma}_{\text{p},\mu}\mathrm{d}t_\mu}{\dot{\gamma}_{\text{p,M}}} \tag{54}$$

where $\dot{\gamma}_{\text{p,M}}$ is the equivalent plastic strain rate that is computed at the maximum load during macro time steps and $\dot{\gamma}_{\text{p},\mu}$ is the equivalent plastic strain rate computed during micro time steps. During the explicit load cycle at micro time t_μ, the response is assumed to be time-independent (elastic). Note that $\dot{\gamma}_{\text{p},\mu}$ is monitored during the load cycle for computing T_{eff} and is not used to update the material state. Therefore, the length of the load period during t_μ does not influence the result.

For determining T_{eff}, the rate of plastic deformation in the mode with the highest initial viscosity is computed at the end of each micro time step and integrated over the load period T. The numerical integration of the integral in Eq. (54) is performed with the trapezoidal rule.

Remark Note that the effective time T_{eff} is computed for each integration point—with a different stress state—and is therefore spatially non-uniform.

3.2. Adaptive cycle jumping

With the time-homogenization scheme, a full viscoplastic update at every micro time step is avoided, which speeds up the simulations of individual load cycles. Computational efficiency can be further improved by simulating multiple cycles at once as will be shown in the following.

The responses of the EGP material model (Kovačević et al., 2024) and the transversely isotropic version (Hofman et al., 2025) (Section 2.2) are mostly frequency independent. This will be demonstrated in Section 3.3. Therefore, when T_{eff} is known after each micro time cycle, we can compute a ratio

$$r_{\text{eff}} = \frac{T_{\text{eff}}}{T} \tag{55}$$

and use this ratio to account for the effective time over multiple cycles

$$\Delta t_{\text{eff}} = r_{\text{eff}}\Delta t \tag{56}$$

where Δt is a time increment that spans multiple cycles and can be chosen with an adaptive stepping scheme based on global convergence rates (Hofman et al., 2024a). The scheme is schematically depicted in Fig. 6. Since plasticity does not evolve during t_μ, the response is elastic and the first half of the explicit load cycle can be mirrored to the second half in order to reduce the number of micro time steps and enhance efficiency. Through time-homogenization and adaptive cycle jumping, multiple cycles can be simulated in a cost-efficient manner.

The time integration of Eq. (26) is performed with an implicit exponential map (Eterovic and Bathe, 1990; Weber and Anand, 1990) to retain plastic incompressibility (Sansour and Kollmann, 1998). By using the effective time increment Δt_{eff}, the deformation gradient $\mathbf{F}_{\text{p}i}$ is computed as

$$\mathbf{F}_{\text{p}i} = \exp\left(\hat{\mathbf{D}}_{\text{p}i}\Delta t_{\text{eff}}\right)\cdot\mathbf{F}^0_{\text{p}i} \tag{57}$$

where $\mathbf{F}^0_{\text{p}i}$ is the deformation gradient at the previous time step.

Remark As pointed out in Kovačević et al. (2024), only the magnitude of plastic deformation is homogenized over the cycle. This is accurate when the direction of plastic flow is constant during the cycle. This means that, under load reversal, when the direction of plastic flow generally changes, inaccuracies may occur with the present scheme. Moreover, since an elastic update is performed during micro time, yielding in the reversed loading direction does not occur, leading to very high equivalent stresses and consequently extremely high equivalent plastic strain rates at the minimum load. As a result, the effective time is unrealistically large and local convergence cannot be achieved. To remedy this, the condition is added that the equivalent plastic strain rate during micro time cannot exceed its value attained at the previous macro time step ($\dot{\gamma}_{\text{p},\mu} \leq \dot{\gamma}^{n-1}_{\text{p,M}}$). This is similar to the condition used in Kovačević et al. (2024), where instead of the equivalent plastic strain rate, the viscosity was limited. By restricting the value of $\dot{\gamma}_{\text{p},\mu}$, it is ensured that the effective time Δt_{eff} does not reach unrealistic values as a result of load reversals. However, the change in sign of the plastic strain is not accounted for and consequently, the present time-homogenization scheme is only accurate under moderate load reversals.

3.3. Verification of time-homogenized viscoplasticity

The time-homogenization scheme is verified by comparing the fully resolved cyclic response of a single trilinear hexahedral element to its time-homogenized response. The single element, with dimensions $1\times1\times1\,\text{mm}$, is subjected to an off-axis sinusoidal load with externally applied load ratio $R = 0.1$, maximum engineering stress level $\sigma_{\max} = 160\,\text{MPa}$ and off-axis angle $\theta_0 = 30°$ (see Fig. 7). The maximum load is reached in $10\,\text{s}$, after which the cyclic loading phase starts. To demonstrate the performance of the method in the case of a full relaxation spectrum, a 24-mode analysis is performed and the material parameters for this analysis are those from Hofman et al. (2025). Furthermore, $n_\mu = 16$ micro time steps are simulated before each macro time step. The influence of the number of micro and macro time steps on the response is determined at the end.

3.3.1. Frequency independence

To assess the assumption that the transversely isotropic viscoplasticity model is mostly frequency independent, three frequencies $f\,(\text{Hz}) = \{0.02, 0.1, 0.5\}$ are simulated. The engineering strain-time histories are depicted in Fig. 8. Since the evolution of maximum and minimum strain values over time are very similar across the range of frequencies, it is confirmed that the effect of frequency on the cyclic response can be ignored, which is important because frequency is not represented in the time-homogenized material update.

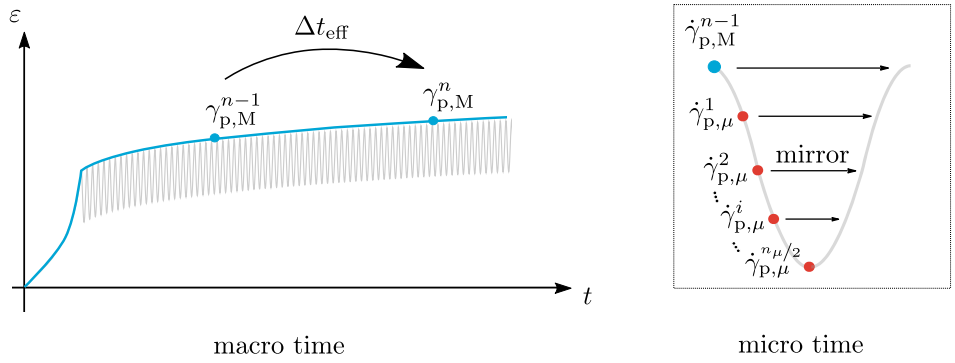

Fig. 6. Time homogenization scheme. The material is updated at macro time (*blue* curve) with an effective time increment Δt_{eff}. The effective time increment is computed by homogenizing the equivalent plastic strain rate during micro time steps (indicated with •).

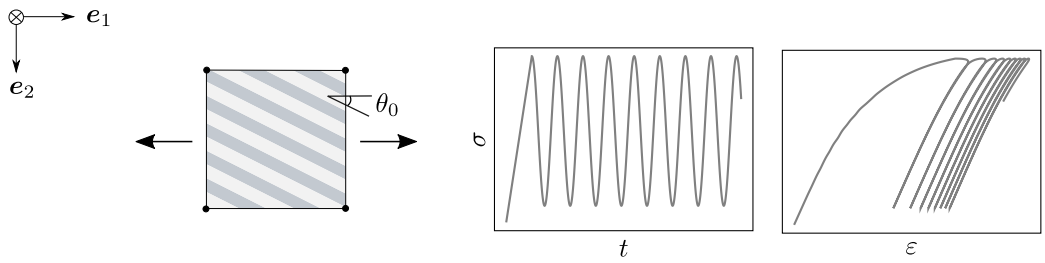

Fig. 7. Off-axis cyclic load test of single element under $\theta_0 = 30°$. A cyclic engineering stress is applied in the e_1-direction with load ratio $R = 0.1$.

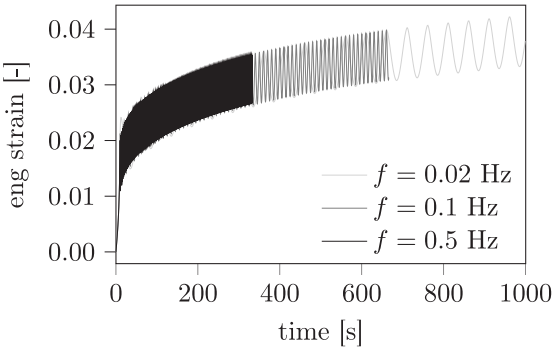

Fig. 8. Fully resolved response with three different frequencies.

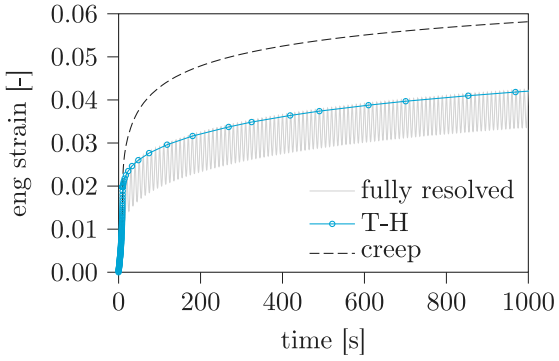

Fig. 9. Time-homogenized response and comparison with the fully resolved and the creep response under constant engineering stress.

3.3.2. *Comparison with fully resolved response*

The time-homogenized response is compared to the fully resolved response. The engineering strain-time histories are depicted in Fig. 9. For comparison, the creep response under constant engineering stress ($\sigma_{\text{max}} = 160\,\text{MPa}$) is added to the diagram. It can be observed that the strain evolution at the maximum load is well captured by the time-homogenization scheme (T-H). Note that, although the history variables are only updated at the maximum load level, the time-homogenization scheme accurately accounts for the cyclic variation of the load through the calculation of Δt_{eff} to perform the time integration. Instead, without the time-homogenization scheme (*i.e.* $\Delta t_{\text{eff}} = \Delta t$), a creep response is obtained and the cyclic load is not accounted for. Under creep, more time is spent at high stress levels, hence more viscoplastic deformations develop in comparison to the cyclic loading case. Furthermore, the fully resolved analysis with frequency $f = 0.1\,\text{Hz}$ reached 1000s with a total of 4434 time steps during the cyclic load phase. With the time-homogenization scheme, only 35 macro time steps were required and for each macro time step, 16 micro time steps (with elastic material behavior) were simulated. The present analyses demonstrate that the two-scale time homogenization scheme significantly increases efficiency while retaining high accuracy. This approach enables high-cycle fatigue analysis with the transversely isotropic viscoplasticity model, which was otherwise infeasible in more complex cases with non-uniform stress fields.

3.3.3. *Micro and macro time step dependence*

The influence of the number of micro time steps n_μ on the accuracy of the time-homogenization scheme is assessed by comparing the simulation results obtained with $n_\mu = \{8, 16, 32\}$. The strain-time response is presented in Fig. 10. It can be observed that for $n_\mu = 16$ and $n_\mu = 32$ the response does not change, whereas for $n_\mu = 8$ inaccurate results are obtained. Therefore, 16 micro time steps are indeed sufficient to capture the evolution of the maximum strain during the cyclic load.

Next, macro time-step dependence is assessed. The viscoplasticity model with implicit exponential map of the deformation gradient update exhibits negligible time step dependence (Hofman et al., 2025). Due to the explicit nature of the time-homogenization scheme under cyclic loads, time-step dependence needs to be re-assessed. For this purpose, the analysis is repeated with the time step size restricted to

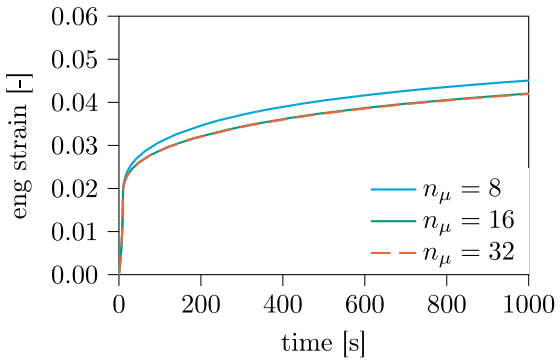

Fig. 10. Time-homogenized response with three different numbers of micro time steps n_μ.

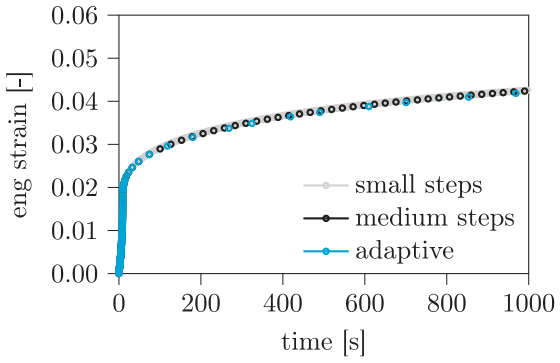

Fig. 11. Time-homogenized response with three different macro time step sizes.

$\Delta t_{\max}\,(\mathrm{s}) = \{5, 20\}$. The results are shown in Fig. 11, along with those obtained with adaptive stepping where the increment was increased up to $\Delta t = 152\,\mathrm{s}$. Since the stress–strain curves overlap, it is concluded that time-step dependence with the two-scale transversely isotropic viscoplasticity model is negligible.

4. Computational analysis of fracture and fatigue in an overmolded T-section

The numerical framework is applied to the simulation of a T-section cut from an overmolded rib-stiffened panel. The effect of two typical processing effects on the short- and long-term mechanical performance of the interface are numerically investigated: local fiber protrusions of the laminate into the rib that occur during thermoforming and non-uniform healing as a result of varying thermal histories along the interface. The modeling approach is discussed in this section and the results under static and cyclic loading are presented in Section 5.

4.1. Processing-induced geometry

We consider an overmolded specimen, made of carbon fiber thermoplastic (CF/PEEK) composite and with laminate lay-up $[90/0]_{10s}$. The laminate, with a total of 20 plies, has a width of 20 mm and the thickness is 2.50 mm. The rib has a length of 18 mm. The width of the rib is 3 mm at the base and reduces to 2 mm at the top. Furthermore, the radius of the rib foot is 0.5 mm.

In this work, we model the laminate with a mesoscopic approach, where each ply is modeled and the local orientation of the fiber direction, due to process-induced wrinkles, is taken into account. Manually meshing a processing-induced deformed geometry is a tedious task. In addition, the fiber vector field needs to be conforming with the

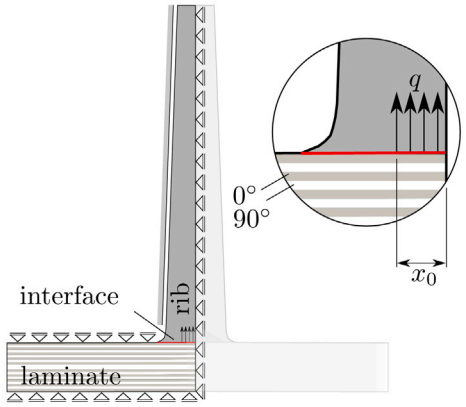

Fig. 12. Computational model of pseudo processing step.

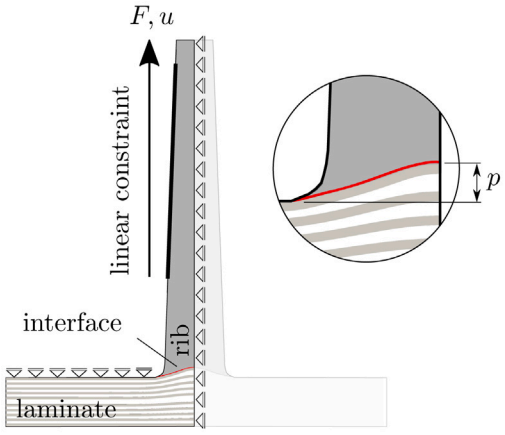

Fig. 13. Computational model of the mechanical test.

final mesh. To obtain a representative shape of the geometry after processing, a practical engineering approach is followed. Prior to mechanical simulation, a "pseudo processing step" is performed to obtain a deformed mesh. For the pseudo processing step, special boundary conditions are used in combination with artificial material properties. The boundary conditions, depicted in Fig. 12, are applied to obtain a local wrinkle. Furthermore, plane-strain conditions are assumed and symmetry is taken into account by modeling only half of the specimen. To drive the deformation, a distributed load q is applied over a width of $x_0 = 0.75\,\mathrm{mm}$. The load is progressively increased until the protrusion height p is equal to 0.5 mm, measured at the center of the rib (see Fig. 13). In addition, the material properties, tabulated in Table 1, are elastic with artificial values. These values are found by trial and error, with the aim to make sure that the 0° plies do not change thickness and have a smooth curvature, while most of the deformation takes place in the 90° plies, similar to what is observed in experiments (Valverde, 2021).

Since a finite strain framework is used, the deformed mesh and fiber vector field at the end of the pseudo processing steps are conforming and can be used in the subsequent mechanical loading step. After the processing step, the mesh and vector field are written to a file and subsequently read prior to the mechanical simulation. The resulting mesh with the pseudo processing step and the initial (undeformed) mesh are shown in Fig. 14.

Obviously, the pseudo processing step is artificial. In a processing–performance chain of models, it can be replaced by a realistic processing step, where first the laminate is heated, formed and solidified. Simulating these steps requires a sophisticated thermomechanical analysis. Such a processing step has been presented in Koptelov et al.

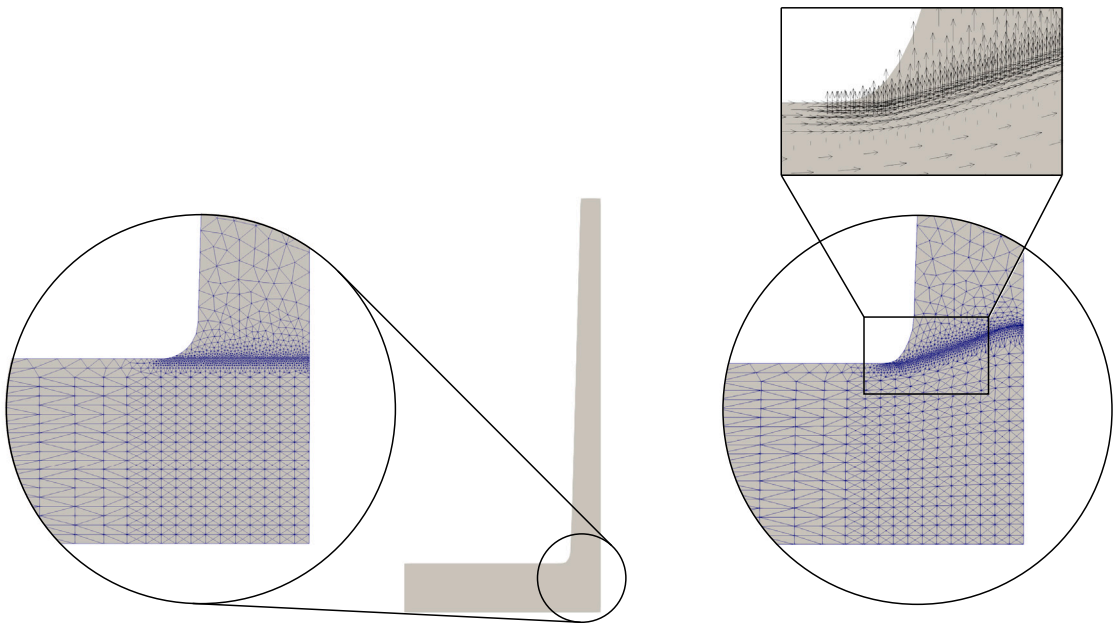

Fig. 14. Meshes used for studying the effects of processing on the geometry of the T-section. Flat geometry (*left*) vs. processing-induced geometry with ply-aligned fiber direction field (*right*).

Table 1
Artificial elasticity parameters for pseudo processing step.

	0°-plies	90°-plies	Rib
E_1	55 GPa	55 GPa	0.55 GPa
E_2	7.4 GPa	0.5 GPa	0.074 GPa
G_{12}	480 GPa	480 GPa	0.048 GPa
ν_{12}	0.016	0.016	0.016
ν_{23}	0.24	0.24	0.24

(2025), where the laminate is simulated in a homogenized sense to improve efficiency. Due to the homogenized assumption, important mesoscopic information for failure analyses (as will be shown later in this paper), such as the local fiber orientation, is not accounted for. In the absence of a detailed processing step, our approach is a convenient method to obtain a processing-induced deformed mesh and corresponding fiber vector field as a result of thermoforming, enabling the study of the effects of a deformed geometry on the mechanical performance.

4.2. Computational model for mechanical test

The computational model for the mechanical pull-off test is shown in Fig. 13. To model the steel tabs that grip the rib during a pull-off test, a linear constraint is applied along the rib edge, starting at a distance of 3 mm above the base of the rib. With the constraint equation, a force-controlled fatigue analysis can be performed. Furthermore, a rib-guard constrains the specimen when the load is applied, which is accounted for by applying homogeneous Dirichlet boundary conditions along the top edge of the laminate.

4.3. Healing profile along the interface

The degree of healing along the interface is a function of the thermal history (Valverde et al., 2018; Akkerman et al., 2020) and can be represented with a healing index D_h, ranging from 0 (no healing) to 1 (fully healed). In Valverde (2021), it is mentioned that the healing values near the edges of the rib are close to zero, because of the thermal boundary conditions: the temperature of the mold tool is relatively low to allow for rapid manufacturing cycles. As a result, interdiffusion of polymer chains across the interface reduces near the edges, leading to a low degree of healing, whereas at the middle of the interface the degree of healing is the highest.

In this manuscript, we qualitatively account for the variation in healing along the interface, through two simplified healing profiles, denoted as "healing A" and "healing B" (see Fig. 15). These profiles are examined for studying the effect of healing on the mechanical response. Following Valverde (2021), the fracture properties for the cohesive zone model for mode $X \in \{\mathrm{I}, \mathrm{II}\}$ are adjusted from the pristine properties $(\cdot)^\infty$ with the healing D_h as

$$f_\mathrm{X} = D_\mathrm{h}\, f_\mathrm{X}^\infty \tag{58}$$

$$G_\mathrm{Xc} = D_\mathrm{h}^2\, G_\mathrm{Xc}^\infty \tag{59}$$

4.4. Local stress ratio

The fatigue cohesive zone model depends on the number of cycles that elapse and accounts for the local stress ratio through the endurance limit calculation (Eq. (19)). When the response is nonlinear, the local stress ratio is not equal to the global load ratio (Raimondo and Bisagni, 2020; Hofman et al., 2024b). Therefore, at macro time steps, when fatigue damage is computed, R must be known.

To retrieve the local stress ratio, the maximum and minimum tractions are monitored during micro time steps. The local stress ratio is computed from the *severity vector* $\mathbf{S} = \left[t_n/f_n, t_{sh}/f_{sh}\right]^\mathrm{T}$ (Joosten et al., 2022):

$$R = \frac{\mathbf{S}_\mathrm{min} \cdot \mathbf{S}_\mathrm{max}}{\left\|\mathbf{S}_\mathrm{max}\right\|^2} \tag{60}$$

where the components of $\mathbf{S}$ are functions of the traction components (t_n and t_{sh}), and the pure-mode strengths (f_n and f_{sh}). After each micro time cycle, the local stress ratio is used to compute fatigue damage at macro time steps through Eq. (19).

4.5. Material parameters

The laminate is modeled with the transversely isotropic viscoplasticity model presented in Section 2.2 using a single mode for simplicity

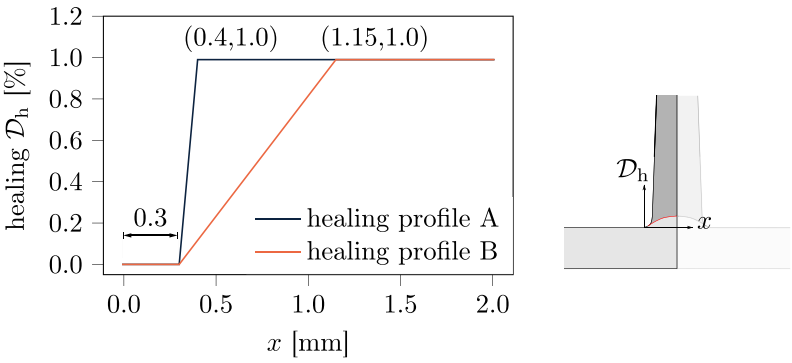

Fig. 15. Different healing profiles along the overmolded interface. A pre-crack of 0.3 mm is assumed at the edges by assigning zero healing.

Table 2
Material parameters of the T-section.

Rib		Laminate					Interface				
elastic		elastic		viscoplastic			fracture			fatigue	
E_1	46 GPa (Valverde, 2021)	E_1	134 GPa (Valverde, 2021)	μ_p	0.053 (Hofman et al., 2025)		f_n^∞	120 MPa (Valverde, 2021)	η	0.95 (Dávila et al., 2020)	
E_2	9 GPa (Valverde, 2021)	E_2	10 GPa (Valverde, 2021)	σ_0	1.71 MPa (Hofman et al., 2025)		f_{sh}^∞	95 MPa (Valverde, 2021)	ϵ	0.2 (Dávila et al., 2020)	
G_{12}	4.3 GPa (Valverde, 2021)	G_{12}	5.2 GPa (Valverde, 2021)	η_0	5.90×10^{29} MPa s (Hofman et al., 2025)		G_{Ic}^∞	2.0 N mm^{-1} (Valverde, 2021)	p	β (Dávila et al., 2020)	
ν_{12}	0.086	ν_{12}	0.016	α_2	1.147 (Hofman et al., 2025)		G_{IIc}^∞	4.0 N mm^{-1} (Valverde, 2021)			
ν_{23}	0.4	ν_{23}	0.24				η_{BK}	2.284			

and more efficient analyses, whereas the rib is considered purely elastic and follows the constitutive equations from Section 2.2.3 without plastic deformations ($\mathbf{F} = \mathbf{F}_e$). The overmolded interface is described with the fatigue cohesive zone model outlined in Section 2.1. The pristine (fully healed) and fatigue cohesive interface properties, the elastic constants of the rib and the laminate viscoplasticity parameters are tabulated in Table 2.

In overmolded thermoplastic composites, the crystallinity of the thermoplastic matrix depends on the processing parameters. As a result, the material parameters of the composite vary depending on the overmoldig process. Ideally, accounting for this would require a sophisticated thermomechanical processing simulation and process-dependent material parameters, which we consider outside the scope of this manuscript.

5. Results

In this section, the pull-off test as described in Section 4 is simulated. The effect of different healing profiles, processing-induced laminate geometries, viscoplastic deformations and boundary conditions are examined under static and cyclic loading.

5.1. Analysis under static loading

Firstly, a static analysis is performed. A constant cross-head displacement rate is applied via the grips and the load per unit length is computed from the reaction force.

5.1.1. Effects of viscoplastic deformations

The effect of viscoplasticity under static loading is shown in Fig. 16, where the force–displacement response is compared to the response without viscoplasticity, with both healing profiles A and B (see Fig. 15). The viscoplastic analyses are performed with displacement rates $\dot{u} = 10^{-3}$ mm s^{-1} and 10^{-5} mm s^{-1}. The crosses in the diagrams indicate mechanical instability: the amount of energy that is released exceeds the amount that is necessary for crack growth, hence the equilibrium path is unstable and cannot be traced in a displacement controlled quasi-static analysis. As can be observed, the effect of viscoplasticity is minimal in the case of healing profile B. However, with improved degrees of healing (healing profile A), the effect of viscoplastic deformations becomes more pronounced. Moreover, when the displacement rate is reduced, there is more time for viscoplastic deformations to accumulate, hence ductility increases and the peak load is delayed.

With a lower degree of healing, the capacity is reduced and fracture in the overmolded interface occurs at lower equivalent stress levels. This is depicted in Fig. 17, where the force–displacement diagrams and the equivalent stress contours on deformed meshes are shown with both healing profiles A and B, under displacement rate $\dot{u} = 10^{-3}$ mm s^{-1}. As expected, with lower degrees of healing, the capacity of the specimen under tensile loading decreases and the equivalent stress is reduced in the laminate and near the crack at the overmolded interface. As a result, viscoplastic deformations play almost no role with low degrees of healing, whereas with improved degrees of healing, stress levels increase and more viscoplastic deformations accumulate.

In the cases studied in Valverde (2021), healing was never fully reached. However, recently another material system was studied in Parsons et al. (2025) and better degrees of healing were observed, leading to a more progressive fracture process during the pull-off test. As shown in this study, under improved levels of healing, viscoplastic deformations become more important to consider. With the aim of optimizing manufacturing process parameters and performance of overmolded composite parts, it is relevant to account for viscoplastic deformations for establishing processing–performance relations through numerical simulations.

5.1.2. Effect of processing-induced geometry

The effect of the processing-induced geometry on the static response is studied with both degrees of healing A and B and displacement rate $\dot{u} = 10^{-3}$ mm s^{-1}. For this purpose, three modeling assumptions regarding the interface geometry are compared: a flat geometry "geometry F", a deformed geometry with initial fiber vector field "geometry D" and a deformed geometry with updated fiber vector field "geometry D$^+$" (see Fig. 18).

The force–displacement curves, corresponding to the three geometries, are shown in Fig. 19. It can be observed that stiffness and capacity of the T-section are larger when the processing-induced geometry is taken into account. As expected and in accordance with Akkerman et al. (2020), Valverde (2021), fiber protrusions (geometry D and D$^+$) improve the strength of the bond due to the curved interface geometry.

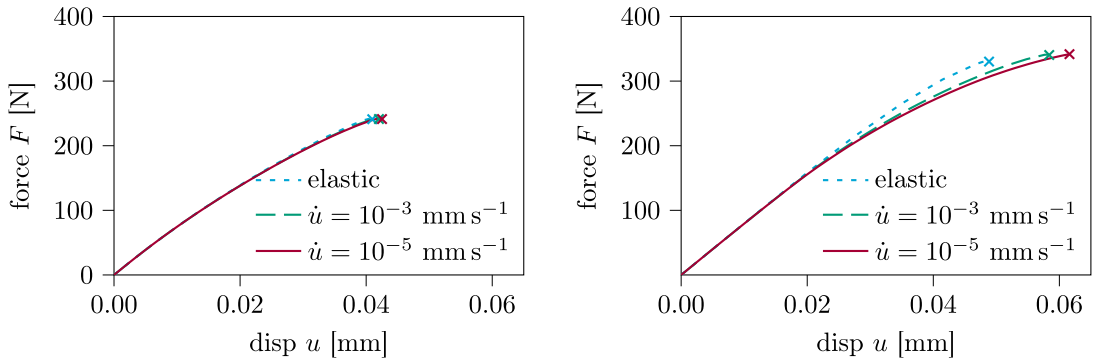

Fig. 16. Force–displacement curves: effect of viscoplasticity on the static response with healing profile B (*left*) and healing profile A (*right*).

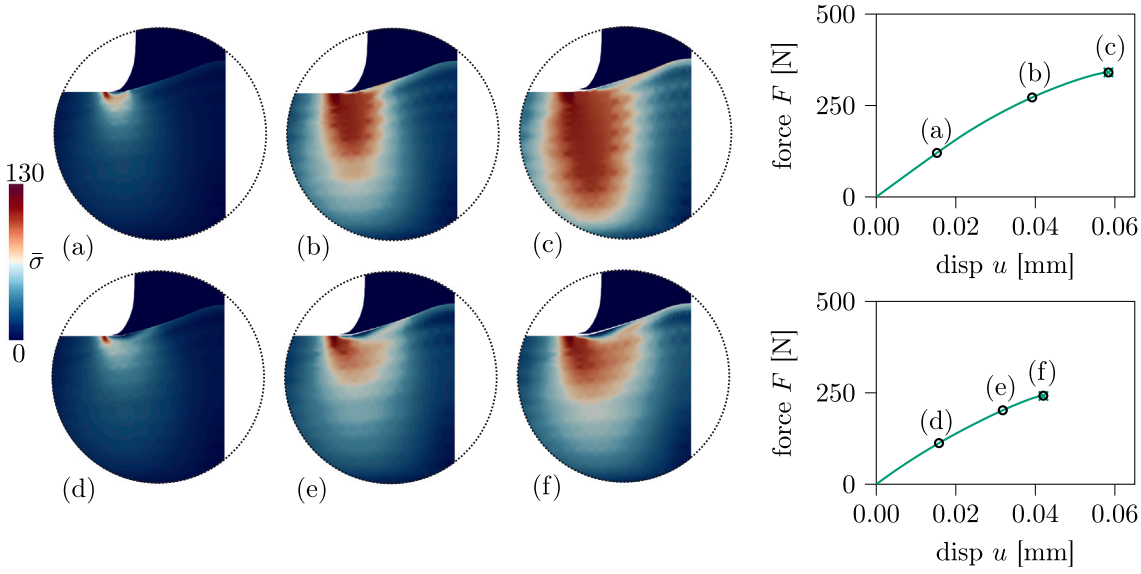

Fig. 17. Evolution of equivalent stress and corresponding force–displacement curves with healing A (*top*) and healing B (*bottom*) at indicated time steps and with displacement rate $\dot{u} = 10^{-3}$ mm s^{-1}.

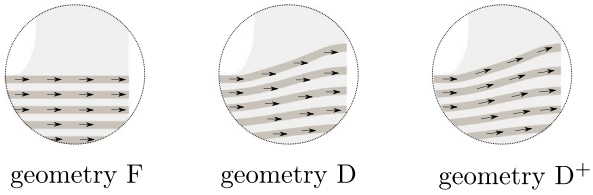

Fig. 18. Three types of laminate geometries are studied: flat geometry (geometry F), deformed geometry with initial fiber vector field (geometry D) and deformed geometry with updated fiber vector field (geometry D$^+$).

In addition, the present analyses demonstrate that accounting for the ply-aligned fiber directions has a significant effect on the strength and stiffness (*cf.* geometry D and geometry D$^+$).

In previous numerical studies of pull-off testing (Valverde, 2021), the laminate was considered a homogeneous medium with a fiber vector field that is aligned with the *undeformed* laminate. This study shows that it is important to take into account the actual fiber direction in the ply, which is captured by the present ply-by-ply mesoscopic analysis.

5.1.3. Effect of boundary conditions

Due to the boundary conditions in the test set-up (see Fig. 13), the laminate is able to bend. To investigate this effect, the analysis is repeated with different boundary conditions. In addition to the standard test set-up studied until now, the laminate is assumed to be fixed (glued) at the bottom, as previously suggested in Song et al. (2024) to prevent bending to occur (see Fig. 20). The force–displacement curves, corresponding to the standard and the glued boundary conditions, are shown in Fig. 21. It can be observed that the boundary conditions mainly affect the stiffness, whereas the strength is very similar among the analyses. In addition, the response is less brittle in the glued case since there is less elastic energy stored that is released during fracture.

5.2. Analysis under cyclic loading

For the cyclic load case, a maximum load level $F_{\max}$ is applied in 10 s, after which a sinusoidal cyclic load with frequency $f = 1$ Hz and load ratio $R = {}^{F_{\min}}/_{F_{\max}} = 0.1$ is maintained (see Fig. 22). The analysis is performed with the time-homogenization scheme presented in Section 3.

The simulation results from the micro time steps are used to compute not only T_{eff} for the viscoplasticity model, but also the local stress ratio R (Section 4.4) for the fatigue damage model. The cycle increment ΔN, used to compute fatigue damage at the overmolded interface (see Eq. (21)) at macro time, is computed through $\Delta N = f \Delta t$.

For analyzing the cyclic response, the displacement $u_{\max}$ at the maximum load is recorded. The displacement rate in macro time $\dot{u}_{\max}$ is also analyzed. Even though this time-homogenized rate does not represent the actual displacement rate in the cyclic experiment, inspecting

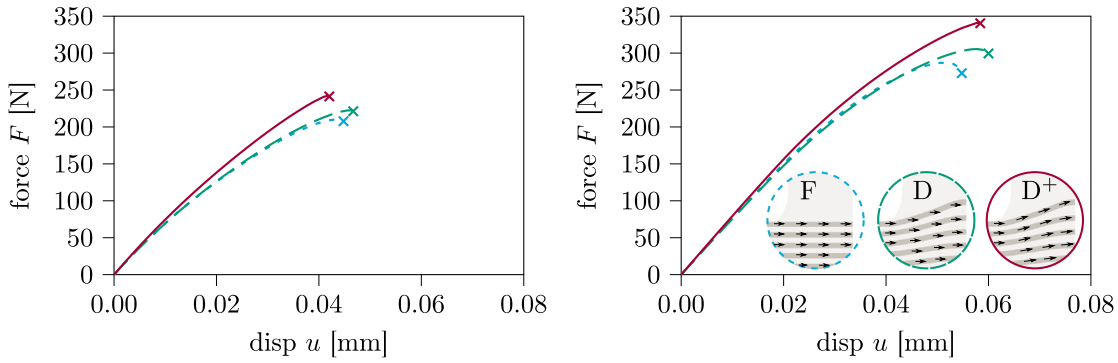

Fig. 19. Force–displacement curves with displacement rate $\dot{u} = 10^{-3}\,\mathrm{mm\,s^{-1}}$: effect of protruded fibers with healing profile B (*left*) and with healing profile A (*right*).

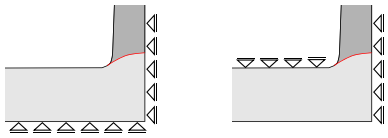

Fig. 20. Sketch of two types of boundary conditions: glued (*left*) vs standard (*right*) test set-up for characterizing interface performance.

$\dot{u}_{\max}$ gives clear insight in the evolution of deformations during the simulation.

5.2.1. *Effect of viscoplasticity*

The effects of viscoplasticity in the laminate on the cyclic response is studied. A force-controlled analysis is first performed with low degree of healing (healing profile B) and with various maximum load levels $F_{\max}\,(\mathrm{N}) \in \{140, 160, 180, 200\}$. The evolutions of the displacement and displacement-rate—at the maximum value of the cyclic load—are shown in Fig. 23. Similar to the static analysis, viscoplastic deformations have a minimal effect on the response with healing profile B. With low levels of healing, the capacity under static loading drops significantly (see Fig. 16). Since the load level in the cyclic test is below the static capacity, fracture occurs before the stresses are large enough to produce significant viscoplastic deformations.

To investigate the effect of the healing profile, the analysis is repeated with improved healing (healing profile A) and maximum stress levels $F_{\max}\,(\mathrm{N}) \in \{210, 230, 250, 285\}$, see Fig. 24. With the higher degree of healing, there is an effect of the viscoplastic deformations, which increases with the applied load level: at increased load levels, stresses are higher and consequently, more viscoplastic deformations develop. As a result, the time-to-failure, which can be identified as the moment when the displacement-rate sharply increases, is delayed (see Fig. 24, *right*).

Apart from the fact that viscoplastic deformations accumulate and interact with crack growth in the overmolded interface, under cyclic loading, viscoplastic deformations also alter the local stress ratio along the interface. To isolate the effects of the local stress ratio, the analysis with $F_{\max} = 285\,\mathrm{N}$ is repeated, but this time with the stress ratio in each integration point set equal to the global load ratio. The displacement histories are shown in Fig. 25 on the left. It can be observed that the viscoplastic deformations have a pronounced effect on the response, while the effect of the local stress ratio is very limited. The local stress ratio history is shown on the right of Fig. 25 for all time steps. Although the local stress ratio is non-uniform, on average it is not much different from the global load ratio, explaining the negligible effect on the fatigue response.

To investigate the effect of the loading type, a displacement controlled analysis is performed, with displacement ratio $R_{\mathrm{disp}} = {}^{u_{\min}}/_{u_{\max}} = 0.1$, applied maximum displacement $u_{\max} = 0.04\,\mathrm{mm}$ and healing profile A. The force histories and local stress ratio along the interface are shown in Fig. 26. It can be observed that under displacement control, the corresponding reaction force at the beginning of the cyclic loading phase is slightly lower in the presence of viscoplastic deformations. Consequently under lower stress levels, the time-to-failure is increased. In addition, the local stress ratio along the profile of the interface is lower than the global displacement ratio. The lower stress ratio results in faster fatigue damage accumulation and thus a decrease in fatigue life in comparison to the case where the stress ratio is chosen equal to the displacement ratio.

The analysis with healing profile A is repeated with various applied maximum displacements $u_{\max}\,(\mathrm{mm}) \in \{0.025, 0.030, 0.035, 0.040\}$ and the time-to-failure for each applied $u_{\max}$ is shown in Fig. 27. From this figure, it is confirmed that viscoplastic deformations are more significant in the low cycle regime and almost negligible in the high-cycle regime. In addition, the time-to-failure curves with the local stress ratio simulations are shifted horizontally towards lower fatigue lives with respect to the curves obtained with a global load ratio.

This study indicates that with lower levels of healing (healing profile B in Fig. 15), viscoplastic deformations have a limited effect on the response of the cyclic pull-off test. However, with improved healing of the interface (healing profile A in Fig. 15), it is important to consider the effects of viscoplastic deformations, mainly in the low cycle regime where the stresses are higher. Therefore, viscoplasticity may be relevant to consider for establishing processing–performance relations to optimize product designs and processing parameters. In addition, it may be important to consider the local stress ratio in the pull-off analyses, particularly in displacement-controlled settings where the local stress ratio and global displacement ratio are not equal. The framework with time-homogenized viscoplasticity with the ability to capture the local stress ratio is suitable for simulating these effects.

5.2.2. *Effect of processing-induced geometry*

The cyclic response with the three geometries depicted in Fig. 18 is assessed. For this purpose, the lower degree of healing (healing profile B) is used with maximum load level $F_{\max} = 160\,\mathrm{N}$. The displacement and displacement-rate histories are shown in Fig. 28. It can be observed that the effect of modeling the mesoscopic geometry—as a result of processing—on the fatigue life is significant. However, similar to what was observed under static loading (see Fig. 19), modeling the protruded interface geometry is not enough, it is also important to account for the alignment of the fibers with the deformed plies, which more than doubles the time-to-failure (*cf.* the response obtained with geometry D and geometry D$^+$ in Fig. 28). The analysis is repeated with various load levels and with both healing profiles A and B. The applied maximum load is plotted against the corresponding time-to-failure in Fig. 29. This figure shows that for both healing profiles across all load levels, modeling the ply-aligned fibers is important.

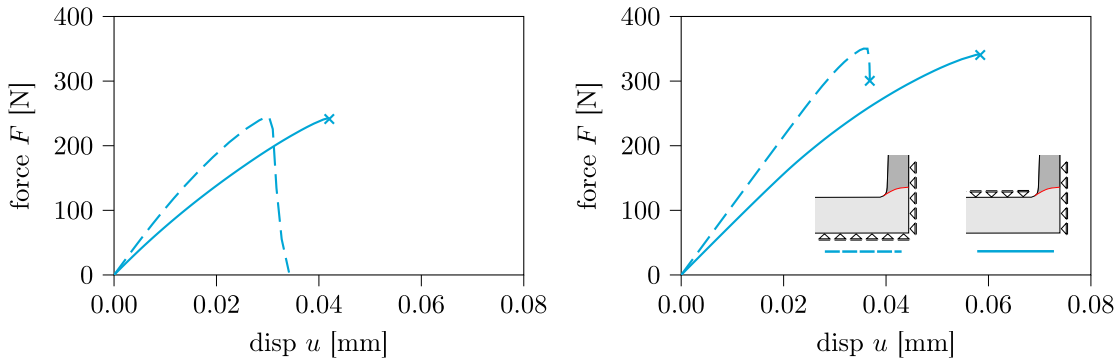

Fig. 21. Force–displacement curves with displacement rate $\dot{u} = 10^{-3}\,\mathrm{mm\,s^{-1}}$: effect of boundary conditions with healing profile B (*left*) and with healing profile A (*right*).

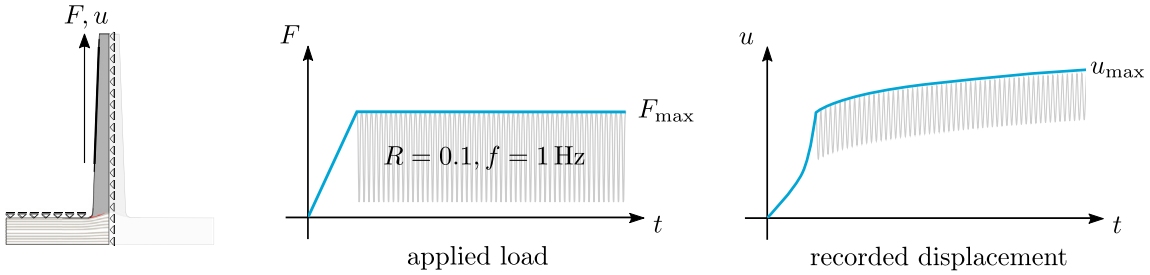

Fig. 22. Analysis under cyclic loading. The maximum load $F_{\max}$ is applied during macro time and the maximum displacement $u_{\max}$ is recorded.

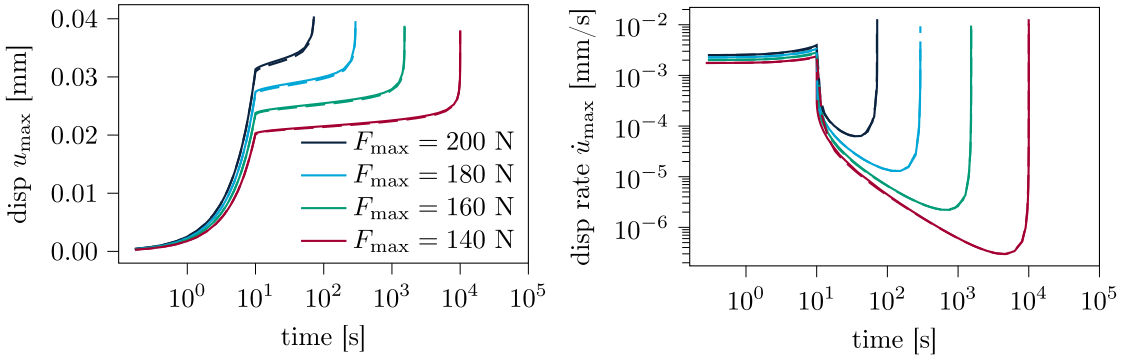

Fig. 23. Response under cyclic load with viscoplasticity (*solid lines*) and without viscoplasticity (*dashed lines*) with healing profile B: displacement history (*left*) and displacement rate history (*right*) at the maximum values of the load.

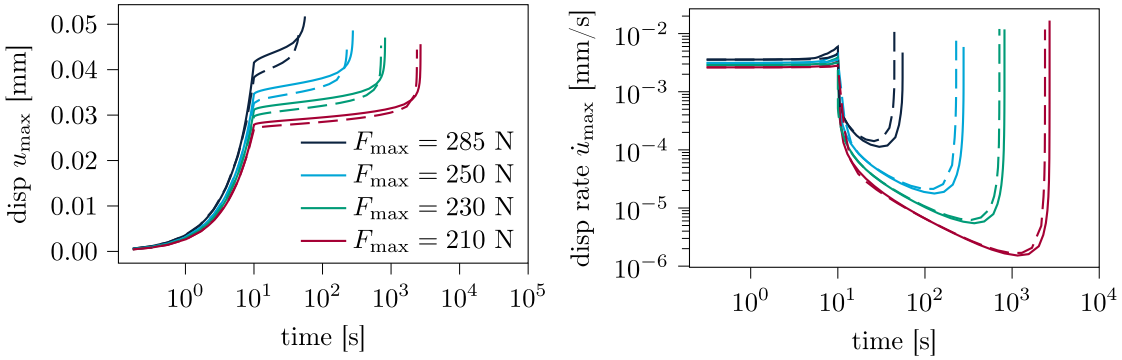

Fig. 24. Response under cyclic load with viscoplasticity (*solid lines*) and without viscoplasticity (*dashed line*) with healing profile A: displacement history (*left*) and displacement rate history (*right*) at the maximum values of the load.

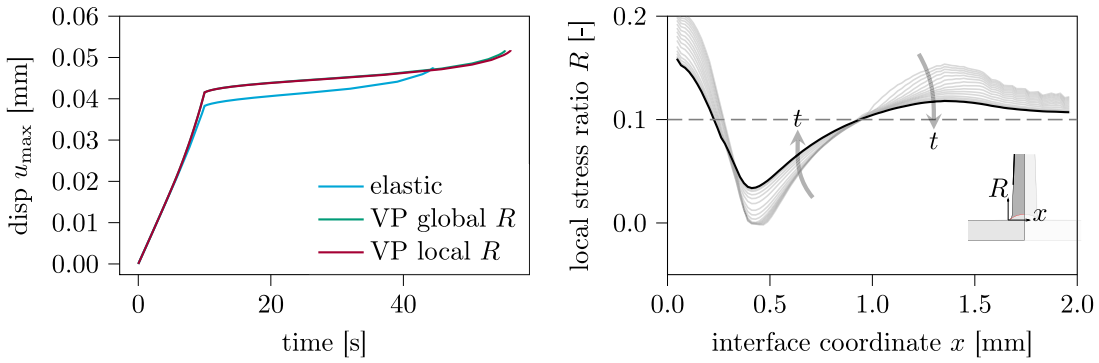

Fig. 25. Effect of viscoplasticity and local stress ratio under force-control with healing profile A and F_{max} = 285 N: displacement–time histories (*left*) and corresponding local stress ratio history with viscoplasticity (*right*). The global load ratio is indicated with a dashed line and each gray line corresponds to a different time step. The last time step is indicated with the black line.

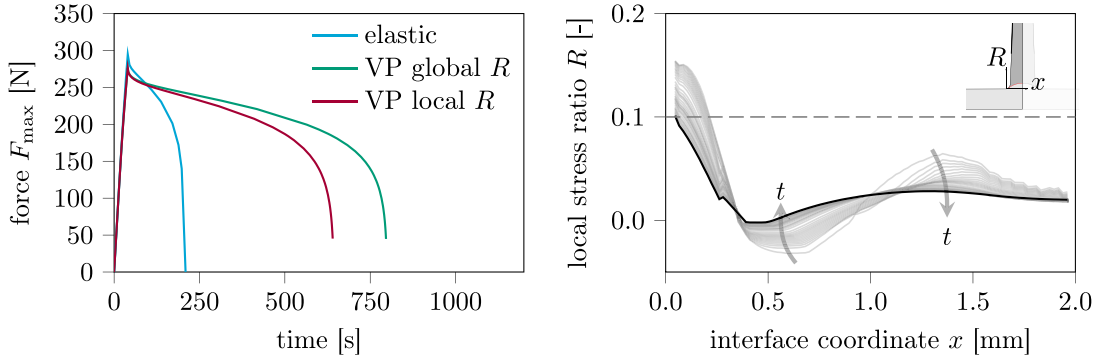

Fig. 26. Effect of viscoplasticity and local stress ratio under displacement-control with healing profile A and u_{max} = 0.4: force-time histories (*left*) and corresponding local stress ratio history with viscoplasticity (*right*). The global displacement ratio is indicated with a dashed line and each gray line corresponds to a different time step. The last time step is indicated with the black line.

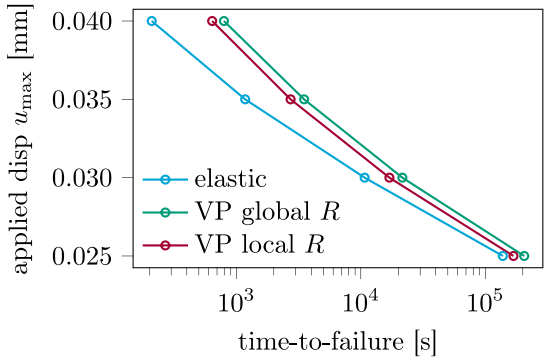

Fig. 27. Time-to-failure under displacement controlled cyclic loading (R_{disp} = 0.1, f = 1 Hz) with various applied maximum displacements: effect of viscoplasticity and local stress ratio.

5.2.3. Effect of boundary conditions

The effect of the boundary conditions on the cyclic response is studied. The analyses with both healing profiles A and B are repeated, but this time the base plate is glued at the bottom (see Fig. 20).

The displacement histories with both types of boundary conditions, healing profile A and maximum load F_{max} = 250 N, are depicted in Fig. 30. It can be observed that the boundary conditions have a strong effect on the cyclic response: the time-to-failure is increased with approximately 71% when bending is prevented. Fig. 31 shows the time-to-failure for each load level with both healing profiles, from which it can be observed that the glued test set-up results in a horizontal shift in the time-to-failure across all stress levels. Under lower degrees of healing (healing profile B) the effect is less significant than under improved healing (healing profile A).

This study demonstrates that the time-to-failure obtained from the pull-off test depends on the test set-up, indicating that S-N curves obtained from pull-off tests do not characterize the interface response under cyclic loads and cannot be used directly as material input in macroscopic failure analyses.

5.2.4. Time step dependence

To assess the time-step dependence of the numerical framework, the analyses with maximum load levels F_{max} = 210 N and 285 N and healing profile A, are repeated with a very large number of time steps. This is achieved by restricting the maximum allowed time step increment: Δt_{max} = 1 s. The displacement rate histories are shown in Fig. 32 and compared to the ones with the adaptive stepping scheme from Fig. 24. It can be observed that time step dependence is negligible. With the adaptive stepping scheme, the time-homogenized micro-macro analyses with F_{max} = 210 N and 285 N are performed with only 17 and 36 macro time steps during the cyclic loading phase, corresponding to 45 and 2682 cycles, respectively. Note that simulating every cycle individually, with 16 micro time steps per cycle, would require 720 and 42912 time steps. The present analyses demonstrate that the numerical framework with time-homogenized viscoplasticity and cycle-dependent cohesive fracture allows for efficient simulations of high-cycle fatigue.

6. Discussion and conclusion

A previously developed numerical framework for simulating fracture and fatigue in composite laminates (Hofman et al., 2024a,b) has been extended to numerically investigate the effects of processing on the mechanical performance of overmolded thermoplastic composites.

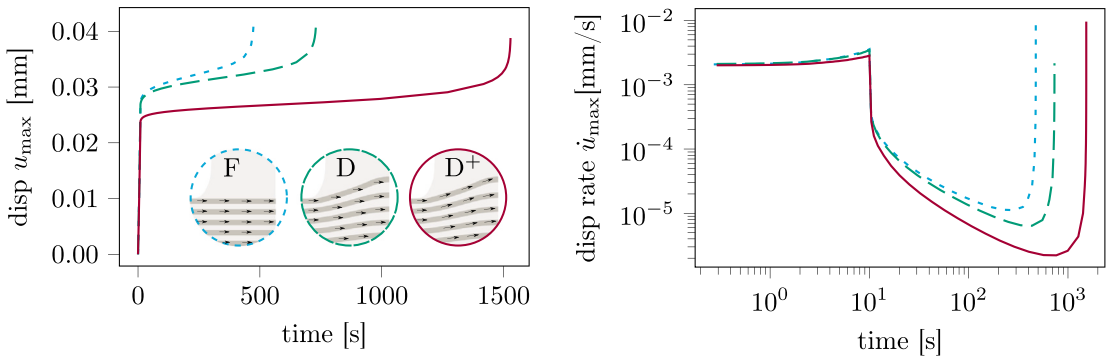

Fig. 28. Cyclic response with different interface geometries F, D, and D$^+$: displacement histories (*left*) and displacement-rate histories (*right*) with healing profile B and maximum load $F_{max} = 160\,N$.

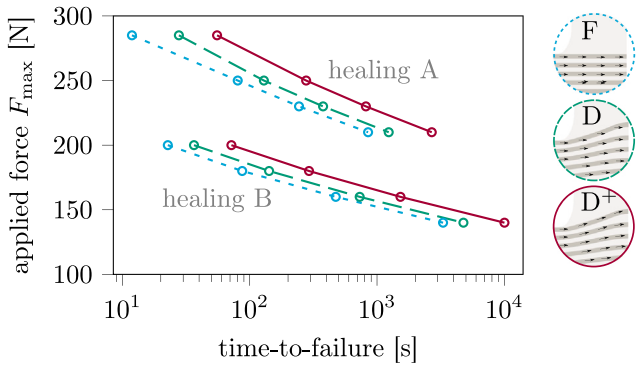

Fig. 29. Time-to-failure under force controlled cyclic loading ($R = 0.1$, $f = 1\,Hz$) with various applied maximum load levels: effect of modeling the protruded fibers with healing profiles A and B.

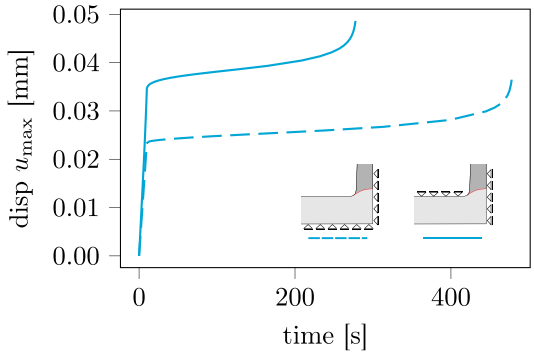

Fig. 30. Displacement–time history: effect of boundary conditions on the cyclic response with healing profile A and $F_{max} = 250\,N$.

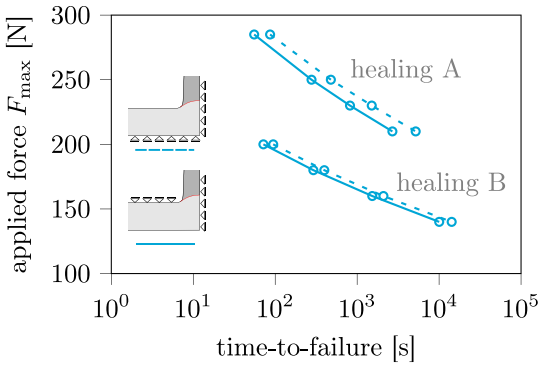

Fig. 31. Time-to-failure under force controlled cyclic loading ($R = 0.1$, $f = 1\,Hz$) at various load levels and healing profiles A and B: effect of different boundary conditions.

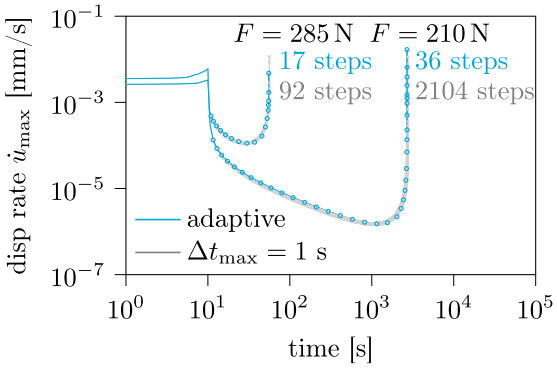

Fig. 32. Displacement-rate histories with two different load levels and step sizes: adaptive stepping vs small time steps ($\Delta t_{max} = 1\,s$). The markers in the plot indicate macro time steps during the cyclic loading phase.

The framework consists of a time-homogenization scheme to efficiently account for the accumulation of viscoplastic deformations during fatigue cycles. A two-scale version of a recently developed transversely isotropic viscoplasticity model for thermoplastic composites (Hofman et al., 2025) has been derived. Furthermore, fatigue at the overmolded interface is modeled with a cycle-dependent cohesive zone model that takes into account the local stress ratio, which is computed during the analyses.

The numerical framework is applied to the static and cyclic analysis of a T-section cut from an overmolded panel. Two typical processing effects are studied: mesoscopic deformations as a result of thermoforming and non-uniform healing due to varying local thermal histories along the interface. To obtain a processing-induced deformed mesh, an engineering approach is proposed by applying special boundary conditions in combination with artificial material properties to generate a mesh with local wrinkles in the laminate. The resulting deformed mesh and fiber vector field are subsequently used to study the effect of the processing-induced geometry on the mechanical performance. The analyses provide the following insights:

- **The process-induced geometry of the interface leads to a better performance**. Besides the curved geometry, it is also important to account for the fiber vector field that is conforming with the plies, which leads to a higher stiffness and capacity under static loading, and longer fatigue life under cyclic loading. This is captured with the presented ply-by-ply modeling

approach where the local non-uniform fiber orientation is taken into account. Therefore, for assessing mechanical performance of the overmolded interface, processing simulations should not only predict the macroscopic geometry, but also provide information on the local fiber orientation. A thickness-homogenized approach for predicting processing effects may not be sufficient for accurate performance assessment, since information is lost about the local fiber orientation.

- **Viscoplasticity affects the strength and fatigue life of overmolded specimens**. With poor healing, the viscoplastic effect is minimal, whereas with good healing, the effect becomes more pronounced. Therefore, for establishing processing–performance relations to optimize processing and product designs, accounting for viscoplastic deformations becomes relevant when a high interface performance is reached. The time-homogenized framework with the two-scale viscoplasticity model is able to account for these viscoplastic deformations under cyclic loading.
- **Viscoplastic deformations alter the local stress ratio**. Under force-controlled loading, the viscoplastic effect is negligible since the local stress ratio on average is close to the global load ratio. However, under displacement-control, the local stress ratio must be accounted for since it cannot be assumed to be equal to the global displacement ratio in the presence of viscoplastic deformations. The macro–micro loading scheme, where the local stress ratio is computed during the analysis, is able to capture this effect.
- **The boundary conditions have a pronounced effect on the response**. Due to the test set-up, the laminate bends, which affects the mechanical response. The effect of gluing the base plate to a support plate on the bottom for characterizing static strength (Song et al., 2024), is investigated under both static and cyclic loading. Under static loading, the effect on the strength is negligible. However, under cyclic loading, the fatigue life is strongly affected by the boundary conditions. Therefore, fatigue properties such as global S-N curves, obtained with the rib pull-off test, cannot be regarded as material properties and directly used as input in macroscopic performance predictions of rib-stiffened overmolded panels.

The development of the numerical framework contributes towards a better understanding of processing effects in overmolded composites. The present studies provided relevant insights, although experimental validation is necessary, especially for fatigue loading, which is currently not available in literature. Furthermore, improvements regarding subcritical intra- and inter-laminar damage, viscoplastic deformations in the short-fiber ribs, accounting for the effects of residual stresses and a more accurate description of the healing profile along the interface are recommended as improvements to the current framework.

CRediT authorship contribution statement

P. Hofman: Writing – original draft, Visualization, Software, Methodology, Conceptualization. **F.P. van der Meer:** Writing – review & editing, Supervision, Project administration, Methodology, Funding acquisition, Conceptualization. **L.J. Sluys:** Writing – review & editing, Supervision, Project administration, Methodology.

Declaration of competing interest

The authors declare that they have no known competing financial interests or personal relationships that could have appeared to influence the work reported in this paper.

Acknowledgments

This research was carried out as part of the project ENLIGHTEN (project number N21010h) in the framework of the Partnership Program of the Materials innovation institute M2i (www.m2i.nl) and the Netherlands Organization for Scientific Research (www.nwo.nl).

Data availability

Data presented in this article is available at the 4TU.ResearchData repository through https://doi.org/10.4121/90f36631-80eb-4d63-b0ac-aad708024e2e.

References

Akkerman, R., Bouwman, M., Wijskamp, S., 2020. Analysis of the thermoplastic composite overmolding process: Interface strength. Front. Mater. 7, http://dx.doi.org/10.3389/fmats.2020.00027.

Benzeggagh, M.L., Kenane, M., 1996. Measurement of mixed-mode delamination fracture toughness of unidirectional glass/epoxy composites with mixed-mode bending. Compos. Sci. Technol. 56, 439–449. http://dx.doi.org/10.1016/0266-3538(96)00005-X.

Bonet, J., Burton, A., 1998. A simple orthotropic, transversely isotropic hyperelastic constitutive equation for large strain computations. Comput. Methods Appl. Mech. Engrg. 162 (1–4), 151–164. http://dx.doi.org/10.1016/S0045-7825(97)00339-3.

Daghia, F., Song, X., Elie, Y., Cluzel, C., 2025. Characterizing adhesion and failure in overmolded T-joint composites with novel isostatic fixtures. In: European Solid Mechanics Conference. Lyon.

Dávila, C.G., 2020. From S-N to the Paris law with a new mixed-mode cohesive fatigue model for delamination in composites. Theor. Appl. Fract. Mech. 106, 102499. http://dx.doi.org/10.1016/j.tafmec.2020.102499.

Dávila, C.G., Rose, C.A., Murri, G.B., Jackson, W.C., Johnston, W.M., 2020. Evaluation of fatigue damage accumulation functions for delamination initiation and propagation. Nasa/Tp–2020-220584.

Eterovic, A.L., Bathe, K.-J., 1990. A hyperelastic-based large strain elasto-plastic constitutive formulation with combined isotropic-kinematic hardening using the logarithmic stress and strain measures. Internat. J. Numer. Methods Engrg. 30 (6), 1099–1114. http://dx.doi.org/10.1002/nme.1620300602.

Fu, L., Zhang, M., Zhai, Z., Jiang, F., 2022. The influence of preheating temperature on the mechanical properties of injection-overmolded hybrid glass fiber reinforced thermoplastic composites. Polym. Test. 105, 107425. http://dx.doi.org/10.1016/j.polymertesting.2021.107425.

Giusti, R., Lucchetta, G., 2020. Modeling the adhesion bonding strength in injection overmolding of polypropylene parts. Polymers 12 (9), 2063. http://dx.doi.org/10.3390/polym12092063.

Giusti, R., Lucchetta, G., 2023. Cohesive zone modeling of the interface fracture in full-thermoplastic hybrid composites for lightweight application. Polymers 15 (22), 4459. http://dx.doi.org/10.3390/polym15224459.

Haouala, S., Doghri, I., 2015. Modeling and algorithms for two-scale time homogenization of viscoelastic-viscoplastic solids under large numbers of cycles. Int. J. Plast. 70, 98–125. http://dx.doi.org/10.1016/j.ijplas.2015.03.005.

Hofman, P., Kovačević, D., van der Meer, F.P., Sluys, L.J., 2025. A viscoplasticity model with an invariant-based non-Newtonian flow rule for unidirectional thermoplastic composites. Mech. Mater. 211, 105507. http://dx.doi.org/10.1016/j.mechmat.2025.105507.

Hofman, P., van der Meer, F.P., Sluys, L.J., 2024a. A numerical framework for simulating progressive failure in composite laminates under high-cycle fatigue loading. Eng. Fract. Mech. 295, 109786. http://dx.doi.org/10.1016/j.engfracmech.2023.109786.

Hofman, P., van der Meer, F.P., Sluys, L.J., 2024b. Modeling of progressive high-cycle fatigue in composite laminates accounting for local stress ratios. Compos. Part A: Appl. Sci. Manuf. 183, 108219. http://dx.doi.org/10.1016/j.compositesa.2024.108219.

Jiang, W., Chen, C., Deng, T., Wang, X., Huang, Z., Zhou, H., Zhou, H., 2022. Effect of material and processing parameters on fiber pinning effect and resultant interfacial bonding strength of CF/PEEK bilayer parts in overmolding process. Polym. Test. 108, 107509. http://dx.doi.org/10.1016/j.polymertesting.2022.107509.

Joosten, M.W., Dávila, C.G., Yang, Q., 2022. Predicting fatigue damage in composites subjected to general loading conditions. Compos. Part A: Appl. Sci. Manuf. 156, 106862. http://dx.doi.org/10.1016/j.compositesa.2022.106862.

Joppich, T., Menrath, A., Henning, F., 2017. Advanced molds and methods for the fundamental analysis of process induced interface bonding properties of hybrid, thermoplastic composites. Procedia CIRP 66, 137–142. http://dx.doi.org/10.1016/j.procir.2017.03.275.

Juvinall, R.C., Marshek, K.M., 2012. Fundamentals of Machine Component Design, fifth ed. John Wiley & Sons, Hoboken, NJ.

Kanters, M.J., Kurokawa, T., Govaert, L.E., 2016. Competition between plasticity-controlled and crack-growth controlled failure in static and cyclic fatigue of thermoplastic polymer systems. Polym. Test. 50, 101–110. http://dx.doi.org/10.1016/j.polymertesting.2016.01.008.

Koptelov, A., Wu, X., Darby, W., Parsons, A., Thomsen, O.T., Hallett, S.R., Harper, L.T., Belnoue, J.P., 2025. Modelling compaction-induced defects in overmoulding of thermoplastic composites. In: Material Forming. pp. 638–645. http://dx.doi.org/10.21741/9781644903599-69.

Kovačević, D., Hofman, P., Rocha, I.B.C.M., van der Meer, F.P., 2024. Unifying creep and fatigue modeling of composites: A time-homogenized micromechanical framework with viscoplasticity and cohesive damage. J. Mech. Phys. Solids 193, 105904. http://dx.doi.org/10.1016/j.jmps.2024.105904.

Kovačević, D., van der Meer, F.P., 2022. Strain-rate based arclength model for nonlinear microscale analysis of unidirectional composites under off-axis loading. Int. J. Solids Struct. 250, 111697. http://dx.doi.org/10.1016/j.ijsolstr.2022.111697.

Kröner, E., 1959. Allgemeine Kontinuumstheorie der Versetzungen und Eigenspannungen. Arch. Ration. Mech. Anal. 4 (1), 273–334. http://dx.doi.org/10.1007/BF00281393.

Lee, E.H., 1969. Elastic-plastic deformation at finite strains. ASMEJ. Appl. Mech. March 36 (1), 1–6.

Liebsch, A., Koshukow, W., Gebauer, J., Kupfer, R., Gude, M., 2019. Overmoulding of consolidated fibre-reinforced thermoplastics - increasing the bonding strength by physical surface pre-treatments. Procedia CIRP 85, 212–217. http://dx.doi.org/10.1016/j.procir.2019.09.047.

Mandel, J., 1972. Plasticite classique et viscoplasticite. In: CISM International Centre for Mechanical Sciences, Springer.

Neveu, F., Cornu, C., Olivier, P., Castanié, B., 2022. Manufacturing and impact behaviour of aeronautic overmolded grid-stiffened thermoplastic carbon plates. Compos. Struct. 284, 115228. http://dx.doi.org/10.1016/j.compstruct.2022.115228.

Oskay, C., Fish, J., 2004. Fatigue life prediction using 2-scale temporal asymptotic homogenization. Internat. J. Numer. Methods Engrg. 61 (3), 329–359. http://dx.doi.org/10.1002/nme.1069.

Parsons, A.J., Molinar-Díaz, J., Koptelov, A., Darby, W., Hooshmand, H., Hernandez Ledezma, F.U., Thomsen, O.T., Belnoue, J.P., Harper, L.T., 2025. Failure modes of CF-PEEK overmoulded onto unidirectionally reinforced CF-LM-PAEK: Multi-scale pull-off testing and microscopy investigation of rib stiffened geometries. Compos. Part B: Eng. 305, 112700. http://dx.doi.org/10.1016/j.compositesb.2025.112700.

Raimondo, A., Bisagni, C., 2020. Analysis of local stress ratio for delamination in composites under fatigue loads. AIAA J. 58 (1), 455–463. http://dx.doi.org/10.2514/1.J058465.

Rocha, I.B.C.M., van der Meer, F.P., Sluys, L.J., 2019. Efficient micromechanical analysis of fiber-reinforced composites subjected to cyclic loading through time homogenization and reduced-order modeling. Comput. Methods Appl. Mech. Engrg. 345, 644–670. http://dx.doi.org/10.1016/j.cma.2018.11.014.

Rodrigues Lopes, I.A., Camanho, P.P., Andrade Pires, F.M., Arteiro, A., 2022. An invariant-based elasto-visco-plastic model for unidirectional polymer composites at finite strains. Int. J. Solids Struct. 236–237, 111292. http://dx.doi.org/10.1016/j.ijsolstr.2021.111292.

Sansour, C., Kollmann, F.G., 1998. Large viscoplastic deformations of shells. Theory and finite element formulation. Comput. Mech. 21 (6), 512–525. http://dx.doi.org/10.1007/s004660050329.

Song, X., Daghia, F., Cluzel, C., Elie, Y., 2024. Influence of boundary conditions on the failure behavior of T-joint shaped overmolded composite structures. In: 21st European Conference on Composite Materials. Nantes, France.

Spencer, A., 1972. Deformations of fibre-reinforced materials. In: Oxford Science Research Papers, Clarendon Press.

Spencer, A.J.M., 1987. Kinematic constraints, constitutive equations and failure rules for anisotropic materials. In: Boehler, J.P. (Ed.), Applications of Tensor Functions in Solid Mechanics. Springer, Vienna, pp. 187–201. http://dx.doi.org/10.1007/978-3-7091-2810-7_10.

Tervoort, T.A., Klompen, E.T.J., Govaert, L.E., 1996. A multi-mode approach to finite, three-dimensional, nonlinear viscoelastic behavior of polymer glasses. J. Rheol. 40 (5), 779–797. http://dx.doi.org/10.1122/1.550755.

Tervoort, T.A., Smit, R.J.M., Brekelmans, W.A.M., Govaert, L.E., 1997. A constitutive equation for the elasto-viscoplastic deformation of glassy polymers. Mech. Time-Dependent Mater. 1, 269–291. http://dx.doi.org/10.1023/A:1009720708029.

Valverde, M.A., 2021. An Improved Description of the Bonding and Consolidation for Overmoulded Thermoplastic Composite Ribbed Plates (Ph.D. thesis).

Valverde, M.A., Kupfer, R., Kawashita, L.F., Gude, M., Hallett, S.R., 2018. Effect of processing parameters on quality and strength in thermoplastic composite injection overmoulded components. In: 18th European Conference on Composite Materials. Applied Mechanics Laboratory.

van Breemen, L.C.A., Klompen, E.T.J., Govaert, L.E., Meijer, H.E.H., 2011. Extending the EGP constitutive model for polymer glasses to multiple relaxation times. J. Mech. Phys. Solids 59 (10), 2191–2207. http://dx.doi.org/10.1016/j.jmps.2011.05.001.

Vogler, M., Rolfes, R., Camanho, P., 2013. Modeling the inelastic deformation and fracture of polymer composites – Part I: Plasticity model. Mech. Mater. 59, 50–64. http://dx.doi.org/10.1016/j.mechmat.2012.12.002.

Weber, G., Anand, L., 1990. Finite deformation constitutive equations and a time integration procedure for isotropic, hyperelastic-viscoplastic solids. Comput. Methods Appl. Mech. Engrg. 79 (2), 173–202. http://dx.doi.org/10.1016/0045-7825(90)90131-5.

Yu, Q., Fish, J., 2002. Temporal homogenization of viscoelastic and viscoplastic solids subjected to locally periodic loading. Comput. Mech. 29 (3), 199–211. http://dx.doi.org/10.1007/s00466-002-0334-y.